

6332

CATALOGED BY ASTIA  
AD NO. \_\_\_\_\_  
401679 1

PER  
TECHNICAL

401679

# AXIAL FIELD EFFECTS IN A MAGNETICALLY DRIVEN SHOCK TUBE

WILLIAM H. HEISER

TECHNICAL REPORT 408

MARCH 29, 1963

17 1963  
ASTIA

MASSACHUSETTS INSTITUTE OF TECHNOLOGY  
RESEARCH LABORATORY OF ELECTRONICS  
CAMBRIDGE, MASSACHUSETTS

The Research Laboratory of Electronics is an interdepartmental laboratory in which faculty members and graduate students from numerous academic departments conduct research.

The research reported in this document was made possible in part by support extended the Massachusetts Institute of Technology, Research Laboratory of Electronics, jointly by the U. S. Army, the U. S. Navy (Office of Naval Research), and the U. S. Air Force (Office of Scientific Research) under Contract DA36-039-sc-78108, Department of the Army Task 3-99-25-001-08; and in part by Contract DA-SIG-36-039-61-G14; additional support was received from the National Science Foundation (Grant G-24073).

Reproduction in whole or in part is permitted for any purpose of the United States Government.

MASSACHUSETTS INSTITUTE OF TECHNOLOGY  
RESEARCH LABORATORY OF ELECTRONICS

Technical Report 408

March 29, 1963

AXIAL FIELD EFFECTS IN A MAGNETICALLY DRIVEN SHOCK TUBE

William H. Heiser

Submitted to the Department of Mechanical Engineering,  
M. I. T., September 12, 1962, in partial fulfillment of the  
requirements for the degree of Doctor of Philosophy.

(Manuscript received November 16, 1962)

Abstract

The effects of a uniform magnetic field normal to the shock front upon shock states and expansion wave properties are theoretically and experimentally investigated for large magnetic-drive fields. One-dimensional theory and several simplifying assumptions are employed to predict the important effects, and a simple method of visualizing the possible shock states is obtained. The restrictions upon shock-wave formation imposed by various types of instabilities are considered. A series of experiments has been performed in a magnetically driven shock tube of annular cross section under conditions approaching the assumptions. Some difficulty was encountered in producing well-formed shocks, and a tentative link with the drive-current breakdown characteristics is established. Observations of well-formed shocks indicate close agreement with shock-transition theory, even when the axial magnetic field exceeds the switch-on value, although the expansion wave properties exhibit large departures from the theory. Some estimates of flow adjustments caused by radius effects and leakage through the boundary layer have been made, and are found to contribute to an understanding of the experimental results.

## TABLE OF CONTENTS

<b>Glossary</b>	<b>iv</b>
<b>I. Introduction</b>	<b>1</b>
<b>II. One-Dimensional Magnetohydrodynamic Shock-Wave Theory</b>	<b>3</b>
2.1 The Shock Layer	3
2.2 The Expansion Wave	8
2.3 Cylindrical Geometry	10
2.4 Quasi-Stationary Assumption	10
<b>III. Description of the Experiment</b>	<b>11</b>
3.1 Equipment	11
3.2 Procedure	18
<b>IV. Experimental Results</b>	<b>21</b>
4.1 Raw Data	26
4.2 Tabulated Results	27
<b>V. Conclusions and Recommendations</b>	<b>37</b>
<b>Appendix I Estimates of the Test Duration</b>	<b>39</b>
<b>Appendix II Absolute Spectral Radiant-Intensity Information</b>	<b>45</b>
<b>Appendix III Auxiliary Equipment</b>	<b>49</b>
<b>Acknowledgment</b>	<b>50</b>
<b>References</b>	<b>51</b>

## GLOSSARY

<u>Symbol</u>	<u>Definition</u>
a	Acoustic speed
b	Alfvén speed
B	Magnetic flux density
c	Magnetoacoustic speed
C	Capacitance
E	Electric field intensity
F	Momentum flux density
G	Mass flux density
H	Stagnation enthalpy
j	Current density
J	Total current
k	Ratio of specific heats
L	Length
m	Mass flux
M	Mach number
n	Electron number density
p	Pressure
P	Radiant flux
r	Radial coordinate
r	Radius
R	Electrical resistance
R	Gas constant
t	Time
T	Temperature
u, v, w	Cartesian velocity components
x, y, z	Cartesian coordinates
V	Electric potential
V	Total speed

## GLOSSARY

<u>Symbol</u>	<u>Definition</u>
$\Delta V$	Volume
$W$	Spectral radiant intensity
$Y$	Bremsstrahlung spectral radiant intensity
$\alpha, \beta, \gamma, \Gamma$	Functions specified in text
$\lambda$	Wavelength
$\mu$	Dynamic viscosity
$\mu$	Magnetic permeability
$\rho$	Mass density
$\sigma$	Electrical conductivity
$\Phi$	Magnetic flux
$\omega$	Angular frequency
$\Delta\Omega$	Spherical angle
<u>Subscripts</u>	<u>Reference</u>
c	Calibration value
c	Contact surface
e	Equilibrium property
f	Fast magnetoacoustic speed
i	Inner radius
J	Current sheet property
L	Loop measurement
o	Outer radius
o	State downstream of drive current
o	Switch-on condition
r	Radial coordinate
s	Measured shock property
s	Slow magnetoacoustic speed
so	Theoretical shock property with zero axial field

## GLOSSARY

### Subscripts

sl

W

x, y, z

1, 2, 3, 4

I, II

### Reference

Theoretical shock property with nonzero axial field

Condition at the shock-tube wall

Cartesian coordinates

Stationary shock states

Wavelengths

## I. INTRODUCTION

The magnetically driven shock tube is capable of producing extremely large velocities and high temperatures, as well as complicated magnetohydrodynamic shock waves, and consequently is the present concern of intensive theoretical and experimental investigation.<sup>1-6</sup> Because magnetohydrodynamic shock waves couple the laws of gasdynamics with those of electromagnetism, the geometry of the shock tube must be carefully chosen to make a theoretical analysis possible. The magnetic annular shock tube (MAST) developed by the Avco-Everett Research Laboratory produces shock waves that approach the one-dimensional model, for which case a complete analysis is available.<sup>1-3</sup> Such a device was constructed in the Magnetogasdynamics Laboratory of the Research Laboratory of Electronics, M. I. T., and an experimental program was initiated to gain an understanding of its actual performance and to explain any major deviations from the theory.

Long before the shock tube was functioning, the effect of a magnetic field normal to the shock front (axial magnetic field) was chosen for investigation. Some of the most interesting magnetohydrodynamic shock phenomena can occur in the presence of a normal magnetic field. These phenomena include increased shock-front velocities, spreading of the expansion wave, and switch-on shock-wave transitions in which part of the drive current flows inside the shock front.<sup>1</sup> The question has also been raised recently about what type of shock transition, if any, is stable when the axial magnetic field exceeds the switch-on value.<sup>2</sup>

Since future shock-tube experiments are likely to incorporate axial magnetic fields for such purposes as acceleration of the shock, stabilization of the boundary layer, or containment of the plasma, it is necessary to determine whether these fields have any unexpected or undesirable effects upon magnetically driven shock-tube performance.

The analyses and experiments reported here were conducted to investigate the effects and answer the questions discussed above.

Section II of this report is devoted to the theory of magnetohydrodynamic shock waves and expansion waves and includes all information necessary for predicting shock-tube performance based upon one-dimensional theory. Section III contains a detailed description of the experimental apparatus, as well as of the experimental procedure. Section IV presents the experimental data in both raw and reduced forms, relates it to the theory, and mentions some of the important observations on the functioning of the experimental equipment. Section V completes the main part of the report by giving conclusions and recommendations.

Appendix I is devoted to some estimates of deviations from one-dimensional theory which arise from radius effects and boundary-layer leakage. Appendix II contains absolute light intensity information for use in measuring emitted experimental light and predicting its magnitude. Appendix III gives a complete list of the auxiliary equipment required for this experiment.

The mks system is employed generally throughout the report, except for some computed values that are stated in more convenient units.

## II. ONE-DIMENSIONAL MAGNETOHYDRODYNAMIC SHOCK-WAVE THEORY

Simple magnetohydrodynamic shock-wave theory will now be outlined, and equations derived which are required for comparison with the experimental results. Some emphasis is placed upon making the phenomena intuitively accessible. In order to emphasize the relationship between the theoretical model and the experimental situation, a brief description of the experiments will be given.

The experiments were designed to furnish shock-velocity and compression-ratio data for high-speed shock waves ( $M_g \gg 1$ ) under the influence of constant magnetic fields perpendicular to the shock front (axial fields). The magnitudes of the axial magnetic field ( $B_x$ ) and experimental gas density ( $\rho_1$ ) were chosen before each experiment from a wide range of possible values. The shock-tube geometry was such that one-dimensional theory is a reasonable first-order approximation, all properties varying only in the axial ( $x$ ) direction.

The magnetically driven shock-wave phenomenon consists of two physically dependent but conceptually separable phenomena: the shock layer and the expansion wave (containing the drive current). Figure 1 qualitatively indicates the important features of the one-dimensional shock wave, as well as the coordinate system used throughout this report. The flow is from  $-x$  to  $+x$  ( $u > 0$ ). Even though the annular shock tube has cylindrical symmetry, Cartesian coordinate system nomenclature is used as a reminder of the assumptions made in the analysis. Careful distinction is maintained between the experimental gas (that is, the gas present in the shock tube before the experiment commences and upstream of the shock front after the experiment commences) and the test gas (that is, the gas present between the shock front and the upstream edge of the expansion wave).

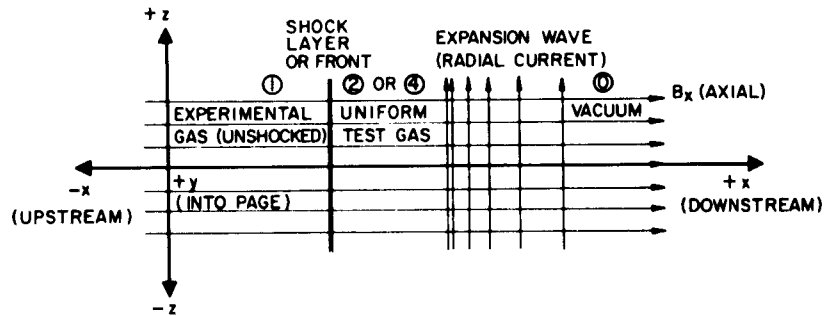


Fig. 1. Coordinate system for one-dimensional shock theory.

### 2.1 THE SHOCK LAYER

#### a. Stationary States

The fluid properties upstream and downstream of the shock layer are stationary and are related through the conservation equations. These properties are independent of

all transport coefficients, which only control the thickness of the shock layer. Shercliff<sup>3</sup> has reduced the conservation equations to the form required for this analysis.

Assuming

- (a) steady flow (shock-stationary reference frame),
- (b) variation in the x-direction only (one-dimensional shock),
- (c) isotropic gas pressure,
- (d) a perfect gas as the working fluid,
- (e)  $\sigma \neq 0$ ,
- (f)  $B_x \neq 0$ ,

Shercliff finds

$$B_y(u-u_0) = \frac{F_y B_x}{G} = \text{constant} \quad (\text{transverse momentum}) \quad (1)$$

$$p + Gu + \frac{B_y^2}{2\mu} = F_x = \text{constant} \quad (\text{Rayleigh}) \quad (2)$$

$$\left(\frac{k}{k-1}\right) \frac{pu}{G} + \frac{u^2}{2} \left(1 + \frac{B_y^2}{B_x^2}\right) = H = \text{constant} \quad (\text{Fanno}) \quad (3)$$

$$B_x = \text{constant} \quad (4)$$

$$G = pu = \text{constant} \quad (5)$$

$$u_0 = \frac{B_x^2}{\mu G} = \text{constant} \quad (6)$$

$$B_z = w = 0 \quad (7)$$

$$\bar{j} = \bar{E} = \bar{V} \times \bar{B} = 0. \quad (8)$$

These relations are also valid within the shock layer, except that  $j_z = \sigma(uB_y - vB_x) \neq 0$ . When  $B_y = 0$  the relations form the usual gasdynamic shock relations, even if  $B_x$  is allowed to approach zero. When  $u = u_0$ , Eq. 6 shows that  $u = \frac{B_x}{\sqrt{\rho\mu}} = b_x$ .

In order to solve these equations outside the shock layer and obtain the possible stationary states for the fluid, it is necessary to specify the values of seven of the functions. Since  $B_x$ ,  $\rho$ ,  $k$ , and  $\mu$  are known in advance of an experiment, the knowledge of any additional three (for example,  $F_x$ ,  $F_y$ , and  $H$ , or  $u$ ,  $p$ , and  $B_y$ ) is required for a solution. Following Anderson,<sup>2</sup> a knowledge of  $F_x$ ,  $F_y$ , and  $H$  is assumed, and the solution of Eqs. 1-3 is represented in three dimensions. Greatest clarification of the experimental problem follows from the choice of  $u$ - $p$ - $B_y^2$  space for this representation (Fig. 2).

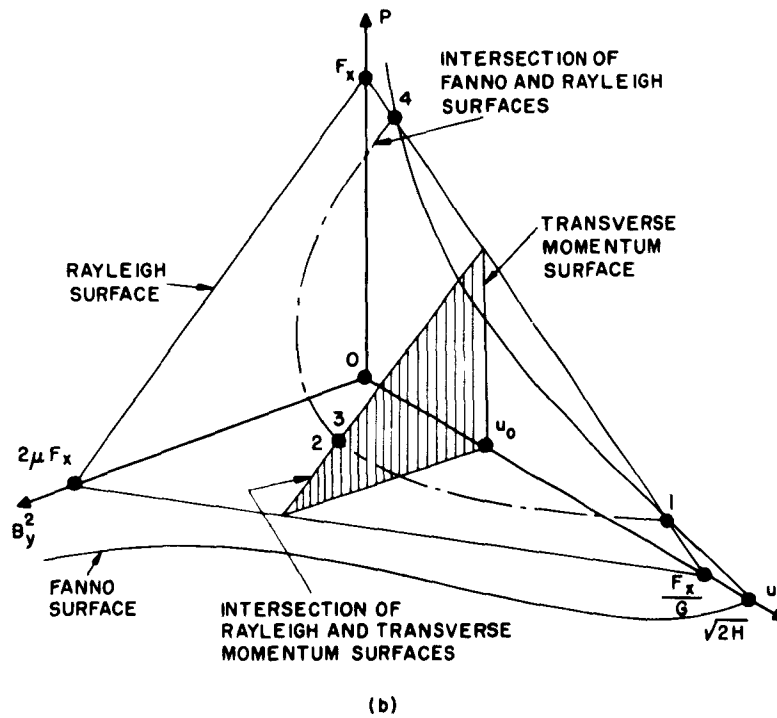
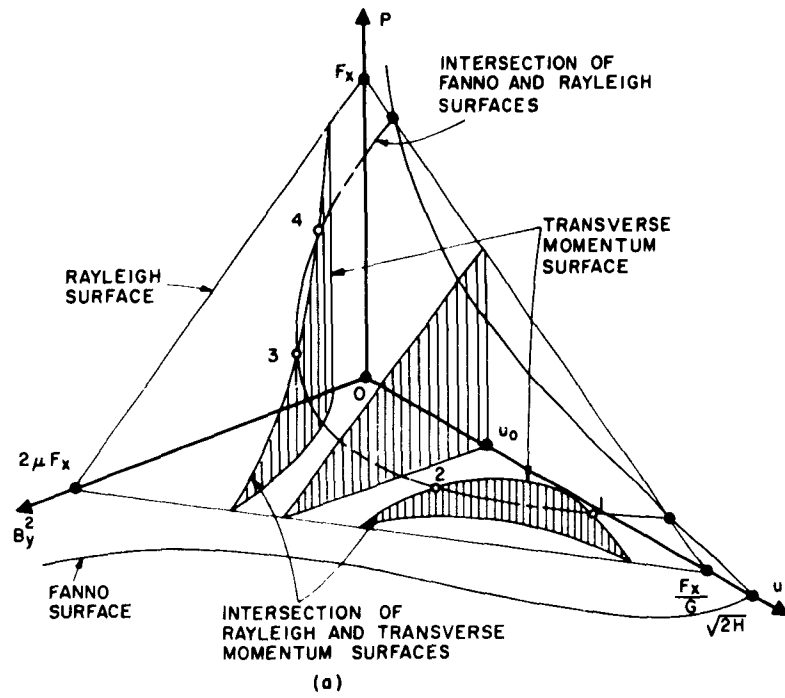


Fig. 2. Graphical representation of stationary shock states. (a)  $B_{y1} \neq 0$ . (b)  $B_{y1} = 0$ .

(i) Transverse momentum surface. This is a cylinder, with generators parallel to the  $p$ -axis. In the  $u$ - $B_y^2$  plane it resembles a hyperbola, the asymptotes being  $u = u_0$  and  $B_y^2 = 0$ . When  $F_y = 0$  it degenerates to the planes  $u = u_0$  and  $B_y^2 = 0$ . Since Eq. 1 has been squared to suit this representation, it must be remembered that  $B_y$  changes sign as  $u$  passes through the value  $u_0$ .

(ii) Rayleigh surface. This is a plane intersecting the coordinate axes at  $u = F_x/G$ ,  $p = F_x$ , and  $B_y^2 = 2\mu F_x$ .

(iii) Fanno surface. This is the most complex of the three, and it will be noted only that this surface is asymptotic to  $u = 0$ , it intersects the  $u$ -axis at its maximum  $u$ -value of  $\sqrt{2H}$ , and it has negative slope and positive curvature in any plane of constant  $B_y^2$ .

Referring to Fig. 2a, it is evident that there are no more than four stationary states for a given set of  $B_x$ ,  $\rho$ ,  $k$ ,  $\mu$ ,  $F_x$ ,  $F_y$ , and  $H$ . They are numbered in the conventional manner, which may be shown<sup>3</sup> to be the direction of decreasing kinetic energy and velocity, and increasing density, pressure, and entropy. The second law of thermodynamics restricts the allowable combinations of the four equilibrium states to six, namely, 1-2, 1-3, 1-4, 2-3, 2-4, and 3-4.

Decreasing  $F_y$  from the value in Fig. 2a causes state 2 to approach state 3 until, when states 2 and 3 coincide,  $F_y = 0$  and  $u_2 = u_3 = b_x$  (Fig. 2b). This is called an Alfvén shock and involves only a change in sign of  $B_y$ . It follows that  $u_2 \geq b_x \geq u_3$ . If  $F_y$  is increased over the value of Fig. 2a until either states 1 and 2 or states 3 and 4 coincide, Eqs. 1-3 reveal that

$$u^4 - u^2(a^2 + b^2) + b_x^2 a^2 = 0 \text{ (magnetoacoustic wave-speed equation).} \quad (9)$$

Here, either  $u_1 = u_2 = c_{fx}$  or  $u_3 = u_4 = c_{sx}$ . Consequently,  $u_1 \geq c_{fx} \geq u_2$ , and  $u_3 \geq c_{sx} \geq u_4$ . The six allowable shock transitions of the diagram may now be characterized:

1-2 (fast shock):  $|B_y|$  increases,  $u_1 \geq c_{fx} \geq u_2 \geq b_x$ ;

3-4 (slow shock):  $|B_y|$  decreases,  $b_x \geq u_3 \geq c_{sx} \geq u_4$ ;

1-3, 1-4, 2-3, 2-4 (intermediate shocks):  $B_y$  and  $(u-u_0)$  change sign.

In this experiment the observed shock velocity ( $u_s$ ) exceeds  $c_{fx}$  in the experimental gas, so that  $u_s$  corresponds to  $u_1$ , and the state of the experimental gas corresponds to state 1 of the theory. Since  $B_{y1} = 0$  and  $B_x \neq 0$ ,  $F_y = 0$ , and the transverse momentum surface takes on the degenerate form discussed above and shown in Fig. 2b. Allowing only  $B_x$  (that is,  $u_0$ ) to vary in Fig. 2b, we see that it is obvious that states 2 and 3 do not exist when  $u_0 \leq u_4$  or  $u_0 \geq u_1$ , so that the only possible shock transition is the gas-dynamic shock (1-4). However, when  $u_4 \leq u_0 \leq u_1$  there exist four equilibrium states, two of which have  $B_y \neq 0$ . Because of the unusual behavior of  $B_y$  in this case, the 1-2 and 1-3 shocks are called "switch-on" shocks, and the 2-4 and 3-4 shocks are called "switch-off" shocks.

The algebra may be simplified by observing that  $M_1 \gg 1$ , whence  $\rho_1 u_1^2 \gg p_1$ , and  $p_1$  may be neglected. It is therefore possible to specify the three required quantities for any given experiment ( $F_x = \rho_1 u_1^2 = \rho_1 u_s^2$ ,  $F_y = 0$ , and  $H = u_s^2/2$ ) and solve the conservation

equations for possible states downstream of the shock layer. The following solutions are easily obtained:

Fast or gasdynamic shock

$$B_{y4} = v_4 = 0 \quad (10)$$

$$\rho_4 = \left( \frac{k_4 + 1}{k_4 - 1} \right) \rho_1 \quad (11)$$

$$p_4 = \left( \frac{2}{k_4 + 1} \right) \rho_1 u_s^2 \quad (12)$$

$$T_4 = \frac{2(k_4 - 1) u_s^2}{(k_4 + 1)^2 R_4} \quad (13)$$

Intermediate or switch-on shock

$$u_2 = u_o = b_{x2} \quad (14)$$

$$\rho_2 = \left( \frac{u_s}{b_{x1}} \right)^2 \rho_1 \quad (15)$$

$$p_2 = \frac{\rho_1 u_s u_o (k_2 - 1)}{2} \left\{ \frac{u_s}{u_o} - 1 \right\}^2 \quad (16)$$

$$T_2 = \frac{(k_2 - 1) u_o^2}{2R_2} \left\{ \frac{u_s}{u_o} - 1 \right\}^2 \quad (17)$$

$$\left( \frac{B_{y2}}{B_x} \right)^2 = (k_2 - 1) \left( \frac{u_s}{u_o} - 1 \right) \left( \frac{k_2 + 1}{k_2 - 1} - \frac{u_s}{u_o} \right) \quad (18)$$

The switch-on shock can only occur when

$$u_o \geq u_4 = \left( \frac{k_4 - 1}{k_4 + 1} \right) u_s \quad (19)$$

or

$$u_s \leq b_{x1} \sqrt{\frac{k_4 + 1}{k_4 - 1}} \quad (20)$$

Since the internal energy upstream of the shock is negligible, these solutions are only functions of the gas properties downstream of the shock. The stationary-state numbering system described above will be used throughout this report.

The u-p-B<sub>y</sub><sup>2</sup> diagram may also be used to represent the effect of simple momentum (ΔF), or of energy (ΔH) sources or sinks in cases in which an algebraic solution would be overly complicated. For example, if we assume that p<sub>1</sub> = B<sub>x</sub> = B<sub>y</sub> = 0 and p<sub>4</sub> and ρ<sub>1</sub>

are known, the effect of a specific enthalpy source of strength  $\Delta H$  may be written

$$\frac{\tilde{u}_1^2}{u_1^2} = \frac{1}{1 - \frac{(k_4^2 - 1)}{2} \frac{\Delta H}{u_1^2}} \quad (21)$$

$$\frac{\tilde{\rho}_4}{\rho_4} = \frac{1}{1 + \frac{(k_4 + 1)\Delta H}{u_1^2}}, \quad (22)$$

where  $\tilde{u}_1$  and  $\tilde{\rho}_4$  are the perturbed values.

#### b. Stability

Finding the possible equilibrium states for a given flow is a simple matter in comparison with determining shock-layer stability. In an extensive treatment of the subject, Anderson<sup>2</sup> examines under similar assumptions the six allowable shock transitions and draws the following general conclusions:

(i) When  $u_o > u_1$  or  $u_o < u_4$  the 1-4 shock is stable.

(ii) When  $u_1 > u_o > u_4$  only the 1-2 and 3-4 shock layers are stable in the evolutionary sense. That is, only these two shock layers emit precisely the number of waves required to conserve all necessary physical quantities at the shock layer. Hence, they can evolve from the accumulation of small waves and can adjust to unsteady flows.

(iii) When  $u = b_x$  (for example, behind a switch-on shock), the shock layer is unstable in the sense that the equilibrium amplitude of the emerging waves is unbounded when a monochromatic wave train of any finite amplitude overtakes the layer.

For  $B_{y1} = 0$  and small values of the axial magnetic field,  $u_o < u_4$ , and the stability arguments (i) agree with the conclusion that the gasdynamic shock (1-4) must appear. For  $B_{y1} = 0$  and large values of the axial magnetic field,  $u_1 > u_o > u_4$ , and the switch-on shock (1-4) should appear (stability argument (ii)). However, the switch-on shock may disintegrate (stability argument (iii)) under the influence of the small waves that are unavoidable in any real experiment. Because the entropy increase is maximum for the gasdynamic shock, the possibility of observing this transition cannot be discounted. Consequently, there is room for speculation as to what type of shock transition will be observed when  $u_1 > u_o > u_4$ , if indeed any shock wave is observed.

## 2.2 THE EXPANSION WAVE

The expansion wave may be regarded as a complex piston that drives the shock wave into the experimental gas. The drive pressure is due to the interaction of the distributed drive current ( $j_z$ ) with its own azimuthal magnetic field ( $B_y$ ), resulting in a volume force of magnitude  $j_z B_y$  in the negative x-direction. The net result is called magnetic driving. Since the drive current may move through the compressed gas both by wave

propagation and diffusion, the resulting mathematical model is intractable. Fortunately, shock-tube magnetic Reynolds numbers are considerably larger than unity (~10 for this experiment); thus the effects of diffusion can be neglected. This is entirely equivalent to the assumption of infinite electrical conductivity.

Under the following assumptions:

- (a) variation in the x-direction only,
- (b) isotropic gas pressure,
- (c) a perfect gas as the working fluid,  $k = \frac{5}{3}$ ,
- (d)  $\frac{1}{\sigma} = 0$ , and

(e) a step function drive current confined to a sheet at  $t = 0$ , Kemp and Petschek<sup>1</sup> computed all necessary expansion-wave properties. A description of the important results for the  $B_{y1} = 0$  case follows.

Any motion of the drive current into the test gas must now depend upon wave propagation. When  $B_x \neq 0$  two longitudinal magnetoacoustic waves arise, their velocities relative to the fluid being  $\pm c_{f(\text{fast})}$  and  $\pm c_{s(\text{slow})}$ . Closer inspection of the property changes across these waves indicates that  $p$  and  $B_y^2$  change in the same direction across the fast wave, and in opposite directions across the slow wave. Since the expansion wave separates two regions for which  $p + \frac{B_y^2}{2\mu}$  is roughly conserved, only slow waves may be present in the expansion wave.

When  $u_0 < u_4$ ,  $B_{y4} = 0$ ,  $c_{fx} = a > u_4$ , and  $c_{sx} = b_x$ . When  $B_x = 0$ ,  $c_{sx} = 0$ , and the expansion wave cannot be spread in the x-direction by the slow wave. There is no physical reason for spreading under this condition, however, for every element of the expansion-wave volume force is directed toward the shock front, tending simply to maintain the shock-front velocity. The drive current remains confined to a single sheet.

When  $B_x \neq 0$  an azimuthal expansion-wave volume force of magnitude  $j_z B_x$  arises. The azimuthal force is balanced only by an inertial force, resulting in an azimuthal acceleration of the fluid. Since the field lines behave as though they were attached to the fluid particles (assumption (d)), the azimuthal motion of the particles within the expansion wave causes a distortion of the field lines. This distortion carries the drive current upstream and downstream, spreading the drive current over a greater quantity of fluid and thereby reducing the azimuthal accelerations. The front edge of the expansion wave now moves relative to the fluid with the speed  $c_{sx4} = b_{x4} < u_4$ , and the fluid that has entered the expansion wave accelerates in the +x-direction. The presence of the axial magnetic field has changed the basic character of the piston. Since Newton's laws must be valid for this system and momentum is being lost through the spreading of the expansion wave, the shock must accelerate ( $p_4$  increases). The computations indicate that this acceleration is slight for the range of values of axial magnetic field available in this experiment (Fig. 20). The computations also indicate that the drive current is largely concentrated at the front of the expansion wave (that is, just downstream of

the test gas), which means that the fluid properties change rapidly there. The decrease of density and temperature through the expansion wave makes assumptions (b) and (d) less reasonable as  $x$  increases. The transverse velocity ( $v$ ) at the downstream edge of the expansion wave is found to be of the order of  $u_1$ .

As  $B_x$  is increased with  $u_0 < u_4$ ,  $b_{x4}$  increases proportionately (Eq. 11), and the front edge of the expansion wave consumes more of the test gas. When  $B_x$  becomes large enough to make  $u_0 = u_4$ , the shock front is no longer separate from the expansion wave. This is seen to be the switch-on condition (Eq. 19).

For even greater values of  $B_x$ , shock-transition algebra indicates several possible alternatives for the test-gas equilibrium condition. Expansion wave theory shows that the gasdynamic shock (1-4) will have no test gas because  $u_4 < b_{x4} = c_{sx4}$ . If the switch-on shock appears,  $u_2 = b_{x2}$  (Eq. 14) and  $b_{x2} > c_{sx2}$  (Eq. 9), and the expansion wave separates from the shock layer and recedes downstream. Currents continue to flow in the shock front, carried there by the fast wave (both  $p$  and  $B_y^2$  increase). As  $B_x$  is increased,  $c_{sx2}/u_2$  decreases continuously, and the amount of test gas increases.

### 2.3 CYLINDRICAL GEOMETRY

The one-dimensional theory is valid for a magnetically driven shock moving axially between two concentric cylinders of radii  $r_o$  and  $r_i$ , provided that

(a) the drive current has azimuthal uniformity,

(b) the drive current source and sink are downstream of the entire expansion wave,

and

$$(c) \frac{2(r_o - r_i)}{(r_o + r_i)} \rightarrow 0.$$

Only (c) presents an experimental problem because  $r_o$  is limited by the size of the equipment, and  $r_o - r_i$  must be large enough to provide sufficient test gas for experimental observation. The value of  $\frac{2(r_o - r_i)}{(r_o + r_i)}$  was reduced to approximately 1/3 for this experiment, which value, according to Patrick,<sup>4</sup> is small enough to make one-dimensional theory approximately correct.

### 2.4 QUASI-STATIONARY ASSUMPTION

The one-dimensional theory is strictly valid only for the case of constant total drive current ( $J$ ). Because the experiment fails to provide a constant  $J$ , the establishment of equilibrium must require a finite amount of time. All shock properties will be computed from the one-dimensional theory by using the instantaneous value of  $J$ . In these experiments the current is fairly constant for approximately 3  $\mu$ sec, and the time required for the acoustic wave to travel from the expansion wave to the shock front is approximately 0.5  $\mu$ sec (fully ionized hydrogen at  $3 \times 10^5$  K). Consequently, the quasi-stationary assumption seems justified.

### III. DESCRIPTION OF THE EXPERIMENT

#### 3.1 EQUIPMENT

The shock-tube consists essentially of two concentric stainless-steel tubes that have been blanked off at both ends to allow the removal of air from the annular volume separating them (Fig. 3). At one end there is a connection to the pumping system. At the opposite end are two tungsten-silver (Elkonite) electrode rings (Figs. 3 and 4) that carry the drive current to and from the experimental gas. They provide the shortest radial path between the two cylinders, and thereby induce the initial breakdown of the experimental gas to take place at a known axial position. Since the shock and expansion wave move away from the electrode end and toward the pump end, the pump end is referred to as "upstream," and the electrode ring end as "downstream," the use of these terms being consistent with the nomenclature of the theory.

Slightly downstream of the electrode ring the experimental gas was introduced through a controlled-leak valve (Fig. 4) and flowed slowly ( $\sim 1$  m/s) toward the pump end. Hydrogen was chosen as the experimental gas for two important reasons. First, the ionization potential for the atomic hydrogen electron is less than 13.6 eV. Consequently, for the anticipated shock velocities ( $\sim 10$  cm/ $\mu$ sec), hydrogen is fully dissociated and ionized,<sup>5</sup> and no complicated secondary ionizations can arise. Second,

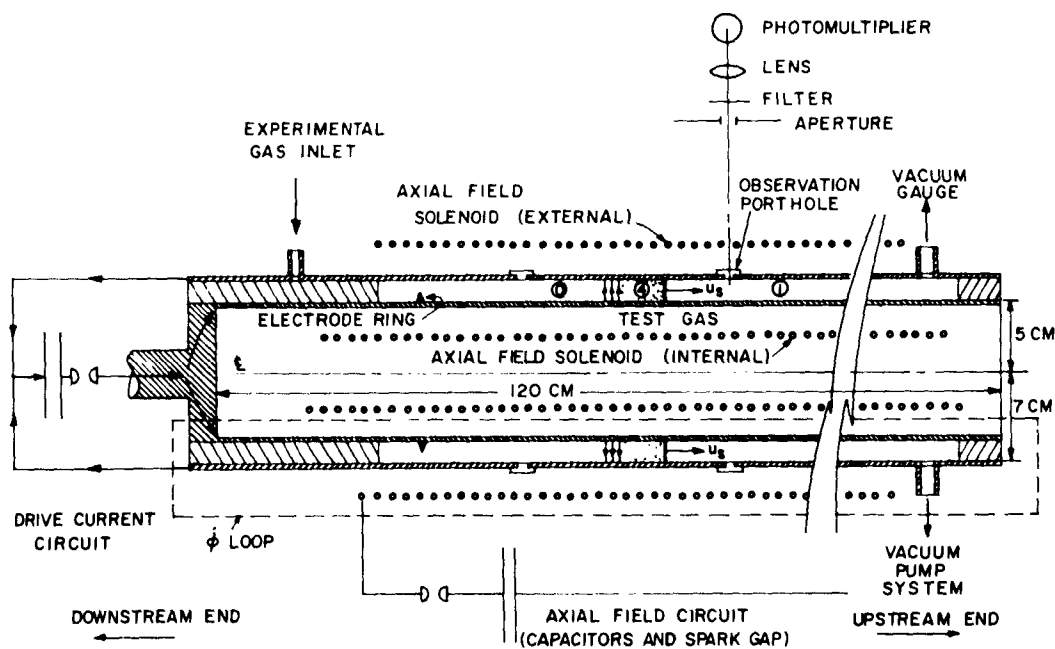


Fig. 3. Schematic representation of the shock tube and auxiliary equipment.

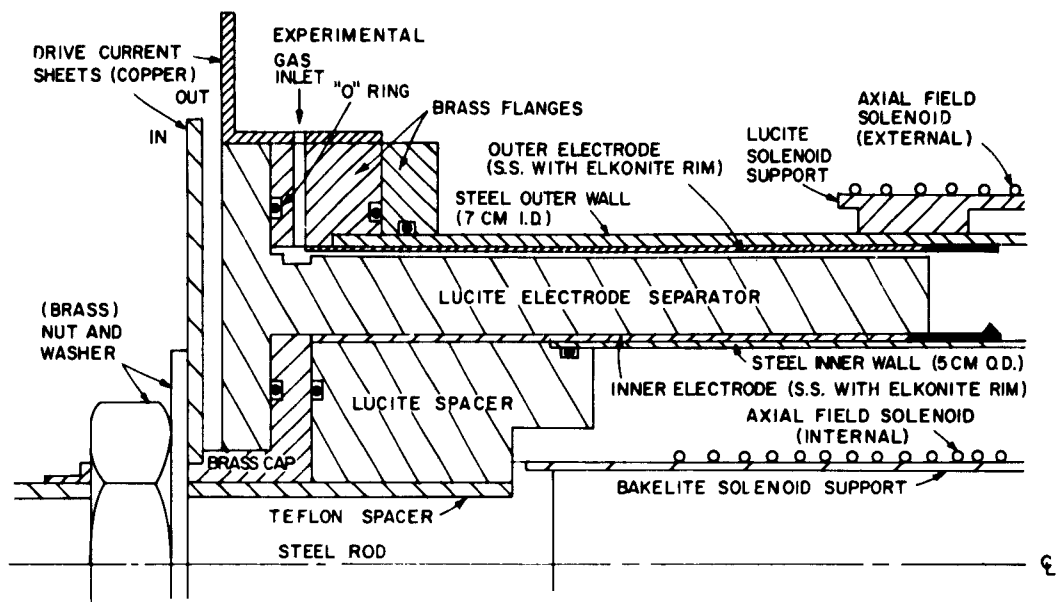


Fig. 4. Cross-section view of the ring-electrode end of the shock tube.

the low density of hydrogen makes large shock-front velocities possible, with the result that the displacement of the shock front during the short period of the experiment ( $\sim 5 \mu\text{sec}$ ) is comparable to the length of the apparatus. Note that the period of the drive current is largely a function of the inductance and capacitance of the external circuit because the inductance does not increase substantially as the drive current moves upstream.

The range of experimental gas pressures ( $p_1$ ) was  $80 \mu$  to  $200 \mu$  ( $\pm 5$  per cent), and measurements were made at a point near the pump inlet (Fig. 3). Viscous-flow calculations indicated a pressure drop of less than  $1 \mu$  from the electrode ring to the pump inlet for these conditions, with the result that axial variation of experimental gas properties could be neglected. Calculations based upon the minimum attainable pressure (with the experimental gas valve closed) and available pump characteristics indicated that impurities in the experimental gas totaled less than 1 per cent by volume.

The electrical currents required for each experiment were stored in capacitor banks and triggered in sequence by high-voltage pulses applied to open-spark gaps (Fig. 5).

The drive-current capacitor bank contained  $172 \mu\text{f}$  (Fig. 7) and supplied an approximately sinusoidal current, with a measured quarter-cycle time of  $4.75 \mu\text{sec}$  and a measured peak value of 49 amps/volt. Since the initial drive-current capacitor bank voltage for all experiments was 4.5 kv, the peak drive current was therefore  $2.2 \times 10^5$  amps ( $\pm 5$  per cent). The inner electrode was positive with respect to the outer

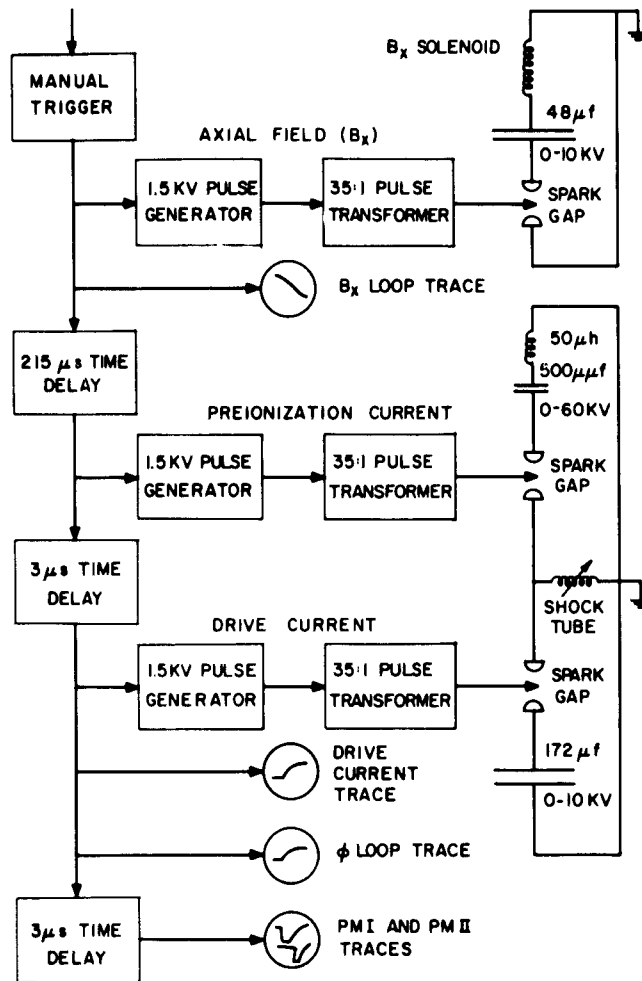


Fig. 5. Electronic sequence and circuit diagram.

electrode. Although no direct experimental evidence has resulted from this experiment, it is possible that the drive-current breakdown behavior is strongly influenced by the mechanical details of the downstream end of the shock tube, particularly the geometry and composition of the drive-current path (Fig. 4). A lucite endpiece was added to the outer cylinder at the extreme upstream end of the shock tube (Fig. 7) to prevent the drive current from shorting out directly across the inner face of the lucite end plate.

The breakdown of the experimental gas at the electrode ring was aided by the free electrons resulting from a small preionization current triggered  $\sim 3 \mu\text{sec}$  in advance of the drive current (Figs. 5 and 8). The preionization current had a peak value of approximately 10 amps and a frequency of approximately 1 mc.



Fig. 6. Over-all view of the experimental equipment. Left to right: equipment rack, containing preionization current charging controls, 215- $\mu$ sec time delay unit, 1.5-kv pulse generators, and safety device controls; oscilloscope monitoring drive-current signal; manual trigger unit; drive-current capacitor bank power supply; axial-field current capacitor bank power supply; drive current capacitor bank (above); shock tube; axial-field current capacitor bank (below); vacuum gauge; oscilloscope monitoring  $\Phi$  and  $B_x$  signals; and oscilloscope monitoring PM I and PM II signals.



Fig. 7. Detail from photomultiplier side. Left to right: stainless-steel inner cylinder; lucite endpiece; vacuum sensing head (above); stainless-steel outer cylinder; lucite axial field solenoid support;  $B_x$  loop (center);  $\phi$  loop (slightly below shock-tube axis); optical openings to test section; preionization current capacitor power supply (above); drive-current capacitor bank, with spark gap and current plates (above); hydrogen bottle (above); and axial-field current capacitor bank and spark gap (below).



Fig. 8. Detail facing photomultiplier side. Left to right, below: preionization current circuit and spark gap; mechanical forepump; diffusion pump; molecular backstreaming trap; and diffusion pump valve. Left to right, above: two photomultiplier units; vacuum sensing head; standard incandescent lamp; two photomultiplier power supplies; and vacuum gauge.

The axial magnetic field was produced by means of a solenoid that was external to the outer cylinder (Figs. 3, 4, 5, and 7). The solenoid was also counterwound inside the inner cylinder in order to reduce the inductance of the circuit. The axial-field current capacitor bank (Fig. 7) had 48  $\mu\text{f}$ , and the current produced an observed mean peak axial field of 0.034 w/m<sup>2</sup> kv ( $\pm 10$  per cent) with a quarter-cycle time of 220  $\mu\text{sec}$ . (This was observed to be longer than the time required for the axial field to penetrate the steel cylinders.) The axial-field current was triggered approximately 215  $\mu\text{sec}$  in advance of the drive current, and the resulting variation of the axial field during the period of the drive current was observed to be less than 2 per cent of the mean peak axial-field value. The axial field was carefully probed for axial and radial variation of magnitude and found to be within 10 per cent of the mean peak field value for all points more than 15 cm upstream of the electrode ring. Fringing of the axial field resulted in larger variations downstream of this point.

The preionization radial electric field and the axial magnetic field act together to make the free electrons of the preionization current move in the azimuthal direction (Hall current),<sup>10</sup> and thereby smooth out any nonuniformities in the azimuthal distribution of the preionization current. This effect varies inversely with the magnitude of the axial magnetic field and encourages a uniform initial azimuthal distribution of the drive current. In the absence of an axial magnetic field, there is no azimuthal particle motion.

Small quartz portholes, located along both sides of the outer cylinder in the horizontal plane containing the shock-tube axis, were provided to allow visual observation of the test gas (Figs. 3 and 7). The portholes were located at 15.3-cm intervals along the axis, the first on each side being 9.0 cm upstream of the electrode ring. The inner surfaces of the portholes were designed to be flush with the inner surface of the outer cylinder in order to prevent them from interfering with the test-gas flow pattern. The inner cylinder was left intact. The outer axial magnetic field solenoid was wound so that the light emitted by the hot test gas could radiate freely within a cone centered about the radius through the portholes.

The intensity of the emitted light was continuously registered by two sensitive, rapid-response photomultipliers that were focused through quartz portholes on a radial portion of the annular experimental space (Figs. 3 and 8).

Well-formed shocks are recognized by their discontinuous nature. The ideal transition time in a coordinate system fixed to the shock tube is the shock-layer thickness divided by the shock velocity.

The expected ideal transition time for this experiment was  $\sim 0.05 \mu\text{sec}$ , but the observed value was much greater, for the following reasons:

1. Even if a step-function light signal were applied to a photomultiplier, the output signal would be delayed by the photomultiplier output circuit rise time. The rise time for the photomultiplier circuits used in this experiment was observed to be  $\sim 0.1 \mu\text{sec}$ .

2. In order to obtain a useful signal from the photomultipliers during the experiments, it was necessary to collect light from a finite volume of test gas. The time required for the shock front to traverse this volume further increased the total rise time. The traversal time was reduced to  $\sim 0.01 \mu\text{sec}$  by placing small apertures over the quartz portholes.

3. The theory presented in Appendix I indicates that the shock front was not located in a plane normal to the shock-tube axis, but was tilted downstream with increasing radius. This tilt could have added as much as  $0.1 \mu\text{sec}$  to the total rise time, but the effect was reduced by tilting the axis of the photomultiplier system approximately  $10^\circ$  away from the radial direction.

Consequently, the expected value of the measured transition time for a well-formed shock was between  $0.1 \mu\text{sec}$  and  $0.2 \mu\text{sec}$ .

Calculations for the radiant emission from fully ionized, hydrogenic gases (Bremsstrahlung) are available.<sup>12, 13</sup> Within the visible wavelength range and for the anticipated test-gas temperatures and zero magnetic field, the Bremsstrahlung spectral radiant intensity (energy/volume/spherical angle/wavelength/time) is proportional to the square of the electron density and is only a weak function of temperature (Appendix II). Two wavelengths were chosen from the high-sensitivity range of the photomultipliers, namely  $3800 \text{ \AA}$  (violet-ultraviolet) and  $5000 \text{ \AA}$  (green), and narrow bandpass optical filter systems (half-width  $< 160 \text{ \AA}$ ) with maximum transmission at each of these wavelengths were used in the experiments. A calibrated incandescent lamp (Fig. 8) was used as a source of known radiant intensity, so that the absolute intensity of the test gas could be determined (Appendix II).

After several trial experiments revealed that the shock arrived almost simultaneously at opposite sides of the shock tube (a rough check of azimuthal symmetry), the two photomultipliers were situated on the same side of the shock tube, at positions  $39.5 \text{ cm}$  and  $54.8 \text{ cm}$  upstream of the electrode ring, and designated PM I and PM II, respectively (Fig. 8). The value of the drive-current maximum usually occurred when the shock front was slightly upstream of PM I, and the typical shock front required  $\sim 2 \mu\text{sec}$  to traverse the distance between PM I and PM II. The variation in drive current was  $\sim 15$  per cent of the peak value during this time. The  $3800 \text{ \AA}$  optical filter was permanently assigned to PM I, and the  $5000 \text{ \AA}$  optical filter to PM II. This assignment was justified by experiments that indicated that the absolute test-gas light signal for each optical filter wavelength was not a function of axial position (that is, of PM I or PM II).

### 3.2 PROCEDURE

Before each series of experiments, the three oscilloscopes (Fig. 6) were calibrated, and each photomultiplier supply voltage was adjusted so that the standard incandescent lamp radiation resulted in an output signal of  $400 \text{ mv}$  ( $\pm 5$  per cent) when the standard lamp was located directly in front of the porthole along the optical axis of the

photomultiplier system. Before each experiment, the oscilloscope scale settings, the initial experimental gas pressure, and the three capacitor bank voltages were adjusted, and the values were recorded. During each experiment, three oscillograms were taken (Figs. 9-17).

The two photomultiplier output signals were simultaneously displayed on a dual-beam oscilloscope, and the traces were recorded on the same oscillogram, the PM I trace having been positioned above the PM II trace (Figs. 9a-17a). The triggering of these traces was delayed until  $\sim 3 \mu\text{sec}$  after the drive-current spark gap was triggered (Fig. 5) in order to record the entire test-gas light intensity profile for both PM I and PM II. The sweep speed was  $1 \mu\text{sec}/\text{cm}$  (left to right), and the vertical scale was chosen as 100, 200, or 500 mv/cm (downward deflection when radiant energy is received), varying as a function of the initial experimental gas pressure.

The rate of change of drive current was monitored by a small-diameter coil of known geometry placed between the copper drive-current plates external to the shock tube (Fig. 7). This signal was integrated ( $RC\omega > 45$ ) before being displayed on a single-beam oscilloscope, and the trace was recorded on an oscillogram (Figs. 9b-17b). The sweep speed was  $1 \mu\text{sec}/\text{cm}$  (left to right), the vertical scale was 100 mv/cm (upward deflection when drive-current flows), and the trace was triggered simultaneously with the drive-current spark gap (Fig. 5).

The axial magnetic field was monitored by a single loop wound around the outer solenoid upstream of PMII (Fig. 7). The potential generated around this loop was equal to the rate of change of axial magnetic field flux through the loop. Since most of the axial field had time to penetrate the steel cylinders, this potential was approximately proportional to the rate of change of the axial field in the experimental gas. Therefore, this was designated as the  $\dot{B}_x$  loop. Data obtained when examining the variation of the axial field as a function of position indicated that the maximum axial field occurred when the  $\dot{B}_x$  loop signal was approximately equal to zero. These data also indicated that the initial value of the  $\dot{B}_x$  loop signal was proportional both to the initial voltage on the axial magnetic field capacitor bank and the peak value of the axial field. Although the initial capacitor-bank voltage was a more accurate means of determining the peak axial field, the  $\dot{B}_x$  signal provided a permanent check on the recorded data. The  $\dot{B}_x$  loop signal was displayed by the upper beam of a dual-beam oscilloscope at a sweep speed of  $50 \mu\text{sec}/\text{cm}$  (left to right) and a vertical scale of either 5 or 10 v/cm, varying as a function of the initial capacitor-bank voltage. The zero for this signal was located on the middle horizontal grid. The oscilloscope trace was triggered simultaneously with the axial-field spark gap (Fig. 5).

The drive-current axial distribution was monitored by a loop around the experimental volume in a plane containing the shock-tube axis (Figs. 3 and 7). The potential generated around this loop was equal to the rate of change of azimuthal flux, and the loop was designated as the  $\dot{\Phi}$  loop. A large initial  $\dot{\Phi}$  signal indicated that some of the drive current had passed from the inner cylinder to the outer cylinder at a point

upstream of the electrode ring; consequently the  $\dot{\phi}$  signal was used to monitor the initial drive-current breakdown of the experimental gas. The first 2-3  $\mu\text{sec}$  of this signal were obscured by high-frequency noise ( $> 20 \text{ mc}$ ), and a filter ( $RC = 4 \times 10^{-8} \text{ s}$ ) was therefore inserted into the oscilloscope input line. The filtered  $\dot{\phi}$  loop signal was displayed by the lower beam of a dual-beam oscilloscope at a sweep speed of 1  $\mu\text{sec}/\text{cm}$  (left to right) and a vertical deflection of 100 v/cm. The oscilloscope trace was triggered simultaneously with the drive-current spark gap (Fig. 5).

The  $\dot{B}_x$  and  $\dot{\phi}$  traces were recorded on the same oscillogram (Figs. 9c-17c), the former appearing above the latter.

The open spark gaps usually broke down within 3  $\mu\text{sec}$  of receiving the triggering pulse, the major exception being the drive-current spark gap at zero axial field. This probably indicates the importance of azimuthal electron drift in breaking down the experimental gas. In many experiments run with zero axial field, data were obtained by using the  $\dot{\phi}$  signal to trigger the photomultiplier oscilloscope. No current trace was obtained in these cases (Fig. 13).

The shock tube required no internal changes between experiments; and before each new experiment the steady flow of experimental gas quickly removed any gaseous impurities that may have resulted from the previous experiment. Each experiment in the series was conducted as soon as the three capacitor banks had been recharged, which required only a few moments.

Experiments were run with the following mean peak values of the axial magnetic field (in  $\text{w}/\text{m}^2$ ): 0.0, 0.017, 0.034, 0.068, 0.102, 0.136, 0.170, 0.204, 0.238.

#### IV. EXPERIMENTAL RESULTS

The well-formed shock has been described in this report as a shock for which the observed shock-layer total transition time (based upon the photomultiplier signal rise time) is less than  $0.2 \mu\text{sec}$ . One of our outstanding experimental observations is that well-formed shocks did not occur in every experiment. The experimental results based only upon photomultiplier oscillogram data may be classified as follows:

1. The majority ( $\sim 65$  per cent) of the experiments failed to produce any recognizable light discontinuity at either photomultiplier (Fig. 9a). These experiments were almost always marked by a 2-mc electromagnetic noise that could not be associated with any known auxiliary circuit. Therefore we concluded that the 2-mc noise was probably associated with the drive current instability that prevented the shock from properly forming.

2. Some of the experiments ( $\sim 10$  per cent) produced a well-formed shock at one photomultiplier and not at the other (Figs. 10a and 11a).

3. Some of the experiments ( $\sim 10$  per cent) produced a discernible, well-formed

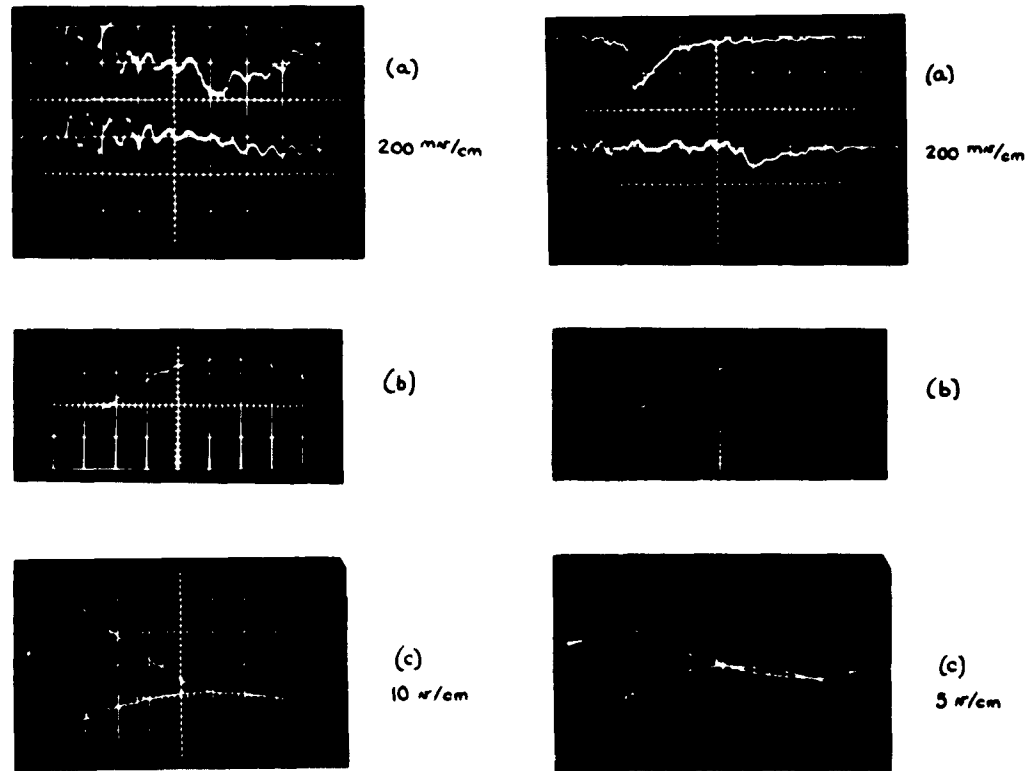


Fig. 9. Data oscillograms.  $B_x = 0.238 \text{ w/m}^2$ ,  $p_1 = 156 \mu\text{H}_2$ .

Fig. 10. Data oscillograms.  $B_x = 0.068 \text{ w/m}^2$ ,  $p_1 = 116 \mu\text{H}_2$ .

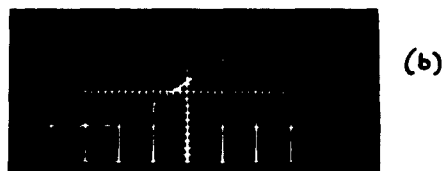
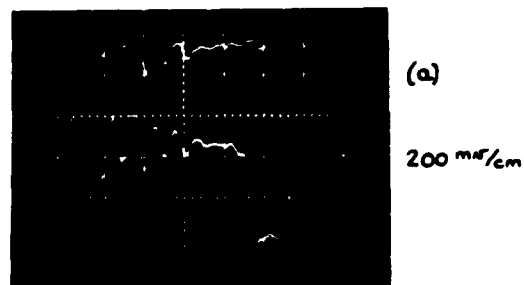


Fig. 11. Data oscillograms.  $B_x = 0.204 \text{ w/m}^2$ ,  $p_1 = 156\mu\text{H}_2$ .



Fig. 12. Data oscillograms.  $B_x = 0.102 \text{ w/m}^2$ ,  $p_1 = 136\mu\text{H}_2$ .

shock despite considerable 2-mc noise, although the amount of the noise in this case was usually less than that found in case 1 (Fig. 12a).

4. In the rest of the experiments (~15 per cent), a well-formed shock was observed at both photomultipliers (Figs. 13a-17a). The noise level was extremely low.

The probability of forming properly and maintaining a shock wave in a given experiment appeared to be a function of peak axial magnetic field and initial experimental gas pressure. As the axial magnetic field was increased from  $0.017$  to  $0.238 \text{ w/m}^2$  (and the azimuthal drift velocity for electrons diminished by a factor of 14), the probability gradually diminished from  $\sim 1/3$  to  $\sim 1/8$ . For the case of zero axial field, the probability was  $\sim 1/6$ . Furthermore, for any given value of axial field, there appeared to be a value of initial pressure below which it was impossible to produce a well-formed shock. This value increased from  $\sim 100 \mu$  to  $\sim 120 \mu$  as the axial field increased from  $0.170 \text{ w/m}^2$  to  $0.204 \text{ w/m}^2$ .

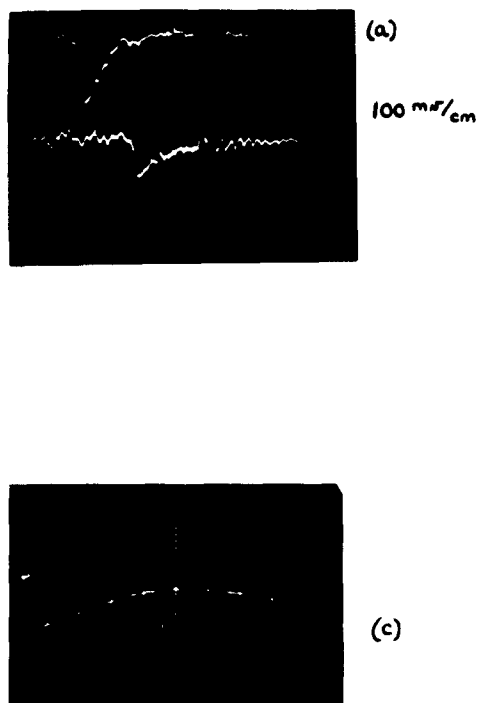
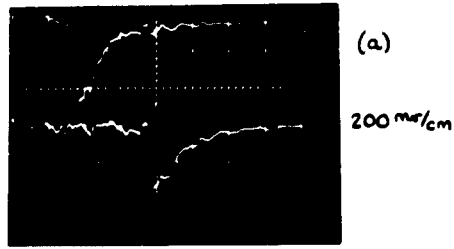


Fig. 13. Data oscillograms.  $B_x = 0.0 \text{ w/m}^2$ ,  
 $p_1 = 112\mu\text{H}_2$ .

These observations concerning probability indicated the influence of the experimental gas conditions on the breakdown characteristics at the electrode rings. (Experiments with zero axial field established that Paschen's minimum occurred at a pressure of  $\sim 800 \mu$ .) Consequently, the probability of producing a well-formed shock could be tentatively linked to the drive-current breakdown characteristics.

Looked at as a whole, the experimental data represent widely varying degrees of success in obtaining well-formed shocks. It might be expected that only the envelope of experimental results approached the theoretical predictions, and it is upon this expectation that the processing of data was based. When at least 20 well-formed shocks were recorded at the value of the axial magnetic field under investigation, the observed shock velocity ( $u_s = \text{distance between successive portholes/passage time of shock front from PM I to PM II}$ ) was compared with the predicted shock velocity ( $u_{s1}$ ). The 10 shock waves indicating the largest percentages of the theoretical velocity were retained for processing. All other data at the chosen value of axial magnetic field were discarded. Data obtained at the maximum axial field ( $0.238 \text{ w/m}^2$ ) constituted the single exception to this procedure; in this case the data from 20 of 40 well-formed shocks were retained for processing. The basic concept was that those shocks that represented the best shock-tube performance probably adhered most closely to the one-dimensional theory



(a)

200 mV/cm

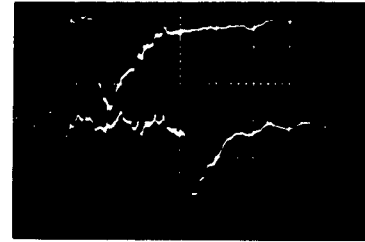


(b)



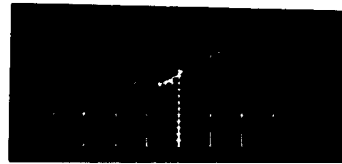
(c)

5 n/cm



(a)

200 mV/cm



(b)



(c)

10 n/cm

Fig. 14. Data oscillograms.  $B_x = 0.034 \text{ w/m}^2$ ,  $p_1 = 136\mu\text{H}_2$ .

Fig. 15. Data oscillograms.  $B_x = 0.170 \text{ w/m}^2$ ,  $p_1 = 128\mu\text{H}_2$ .

because fewer unexpected influences (for example, arc instabilities) had acted upon them.

This procedure required a method of computing the theoretical velocity as a function of experimental parameters. When the axial magnetic field is zero, one-dimensional theory predicts that the drive-current sheet will behave as an impenetrable piston of

known downstream pressure  $\left(p_4 = \frac{B_{yo}^2}{2\mu}\right)$ , and the usual gasdynamic shock relations will be valid. Hence, for  $k_4 = \frac{5}{3}$ ,

$$u_{Bo} = \sqrt{\frac{4}{3} \frac{p_4}{\rho_1}} = B_{yo} \sqrt{\frac{2}{3\rho_1\mu}} \quad (23)$$

Since

$$B_{yo} = \frac{\mu J}{2\pi r}, \quad (24)$$

$$u_{Bo} = \frac{J}{\pi r} \sqrt{\frac{\mu}{6\rho_1}} \quad (25)$$



(a)

200 mV/cm

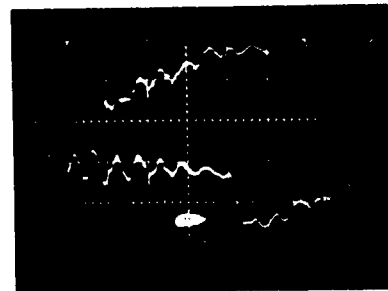


(b)



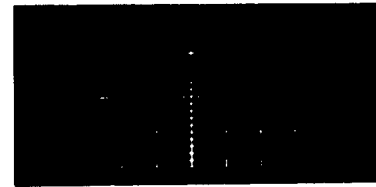
(c)

10 V/cm

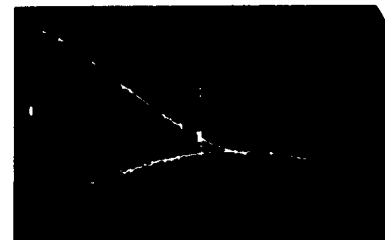


(a)

100 mV/cm



(b)



(c)

10 V/cm

Fig. 16. Data oscillograms.  $B_x = 0.238 \text{ w/m}^2$ ,  $p_1 = 136\mu\text{H}_2$ .

Fig. 17. Data oscillograms.  $B_x = 0.238 \text{ w/m}^2$ ,  $p_1 = 152\mu\text{H}_2$ .

When the axial magnetic field was not zero,  $u_{s1}$  was obtained by combining Eq. 25 with the computed information of Fig. 20.

Since  $u_{s1}$  was computed from measured quantities, the important errors were carefully assessed to allow a fair comparison of  $u_{s1}$  with  $u_s$  as follows:

1. In Eq. 25 the first influence of the cylindrical geometry upon the experiment was found. The proper choice for a numerical value of  $1/r$  was probably between  $1/r_o$  and  $1/r_i$ . The mean value  $\frac{r_i + r_o}{2r_i r_o}$  was used in the calculations. The maximum deviation of  $u_{s0}$  because of this particular choice of  $1/r$ , therefore, should not have exceeded  $\frac{r_o - r_i}{r_o + r_i} \times 100 = 17$  per cent.

2. The value of  $p_1$  was computed from the measured value of  $p_1$  and the perfect gas law, under the assumption that  $T_1 = 273^\circ\text{K}$ . Since the vacuum gauge was calibrated

at room temperature, the computed value of  $1/\sqrt{\rho_1}$  might have been 5 per cent below the actual value.

3. The boundary-layer theory of Appendix I indicates a 14 per cent decrease in shock velocity when the test gas slug length is in equilibrium.

Since these errors were independent, it was possible to conclude the fact that the expected value of  $u_g$  for zero axial field should have been between  $0.7 u_{g0}$  and  $1.2 u_{g0}$ .

If we assume that (a) there was no axial magnetic field; (b) the experimental gas was in an unexcited state; and (c) the test gas was fully ionized, Eqs. 21 and 22 show that for this experiment (hydrogen gas,  $u_1 = 10 \text{ cm}/\mu\text{sec}$ ),  $\frac{\tilde{u}_1}{u_1} \cong 0.95$ , and  $\frac{\tilde{p}_4}{\rho_4} \cong 1.5$ .

Under experimental conditions similar to those reported here, Patrick<sup>4</sup> found  $\frac{\tilde{p}_4}{\rho_4} \cong 1$ ,

and Weise et al.<sup>7</sup> found  $\frac{\tilde{p}_4}{\rho_4} \cong 0.9$  and  $T_4 \cong 3 \times 10^5 \text{ }^\circ\text{K}$ . Weise et al. conclude that this is the result of the delivery of excitation energy to the experimental gas by means other than shock heating (for example, ultraviolet radiation from the drive current) and in sufficient amounts to ionize the experimental gas before the arrival of the shock front.

#### 4.1 RAW DATA

##### a. Photomultiplier Oscillograms (Figs. 12a-17a)

The decrease of test gas density (that is, light intensity) at the upstream edge of the expansion wave was rapid, just as the one-dimensional theory qualitatively predicted. The observed length of the test gas slug was approximately 5 cm for all initial conditions, which was consistent with the boundary-layer leakage theory (Appendix I), but over far too wide a range of axial fields to have been anything more than a coincidence. No precursor light was observed at these wavelengths. The success or failure of a given experiment in producing a well-formed shock could only be detected on the photomultiplier oscillogram.

##### b. Drive-Current Oscillograms (Figs. 12b-17b)

The drive-current oscillograms recorded the spark gap and electrode ring breakdown delay time and breakdown noise. The drive current was fairly sinusoidal. The variation among experiments was negligible.

##### c. $\dot{B}_x$ Oscillograms (Figs. 12c-17c)

The interruption of the  $\dot{B}_x$  signal at  $\sim 220 \mu\text{sec}$  was caused by drive-current breakdown noise, and therefore provided an additional timing check. Even though the  $\dot{B}_x$  loop was in a plane normal to the shock-tube axis, and even though it was more than four loop diameters distant from the electrode ring, the magnitude and duration of the interruption was proportional to the 2-mc noise found on the photomultiplier traces.

d.  $\dot{\Phi}$  Loop (Figs. 12c-17c)

The  $\dot{\Phi}$  loop was originally designed to check on the drive-current breakdown, but, as shown below, it yields additional information.

Under the assumptions that (a) the drive current has azimuthal symmetry; (b) the axial distribution may be approximated by  $\alpha J$  crossing through the experimental gas at the upstream end and  $(1-\alpha)J$  crossing at the electrode end (an observation made after examining the disassembled shock tube); and (c) that the average drive current element moves upstream with the velocity  $u_J$  (pseudo-current velocity), Faraday's law reveals that

$$V_L = \frac{\mu J}{\pi} \left( \frac{r_o - r_i}{r_o + r_i} \right) \left\{ \alpha \omega L \cos \omega t + (1-\alpha) \left[ u_J \sin \omega t + \omega \cos \omega t \int_0^t u_J dt \right] \right\} \quad (26)$$

where  $V_L$  is the magnitude of the  $\dot{\Phi}$  signal,  $L$  is the length of the shock tube, and  $\omega$  is the frequency and  $J$  the peak value of the sinusoidal drive current. Thus, at  $t = 0$

$$\alpha = \frac{\pi V_L}{\mu L J \omega} \left( \frac{r_o + r_i}{r_o - r_i} \right). \quad (27)$$

Since  $V_L$  was observed to be  $< 100$  v at  $t = 0$ , Eq. 27 shows that  $\alpha$  for this experiment was  $< 0.03$  and may therefore be neglected. Equation 26 may be rearranged with  $\alpha = 0$  to yield (at peak current)

$$u_J = \frac{\pi V_L}{\mu J} \left( \frac{r_o + r_i}{r_o - r_i} \right). \quad (28)$$

For  $V_L = 100$  v,  $u_J$  was  $0.70$  cm/ $\mu$ sec for this experiment.

Equation 26 plus the quasi-stationary assumption (section 2.2) show that  $V_L$  is expected to be similar to  $\sin^2 \omega t$  for  $t < \pi/2\omega$ , whereas the oscillograms revealed that  $V_L$  was proportional to  $\sin \omega t$  for  $t < \pi/2\omega$ . This discrepancy indicated that the actual drive-current axial distribution may have differed from the prediction of the one-dimensional theory. Although a 4-mc noise was frequently observed on this trace, the 2-mc noise was never observed.

#### 4.2 TABULATED RESULTS

The reduced data are often divided into subcritical ( $0-0.102$  w/m<sup>2</sup>) and critical ( $0.136-0.238$  w/m<sup>2</sup>) axial magnetic field groups, in order to separate those shocks without the switch-on alternative from those shocks with the switch-on alternative.

##### a. Observed Shock Velocity (Figs. 18-20)

The observed shock velocity ( $u_s$ ) is compared with  $u_{s0}$  (not  $u_{s1}$ ) as a function of both  $p_1$  and  $B_x$  in Figs. 18 and 19. The estimated maximum error in the measurement of  $u_s$  is 10 per cent.

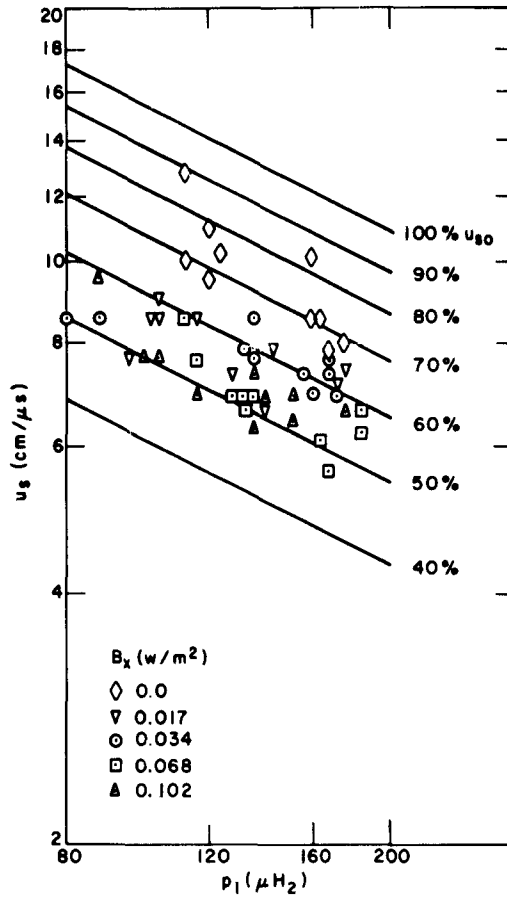


Fig. 18.  $u_s$  and  $u_{s0}$  as functions of  $B_x$  and  $p_1$ ,  $B_x \leq 0.102 \text{ w/m}^2$ .

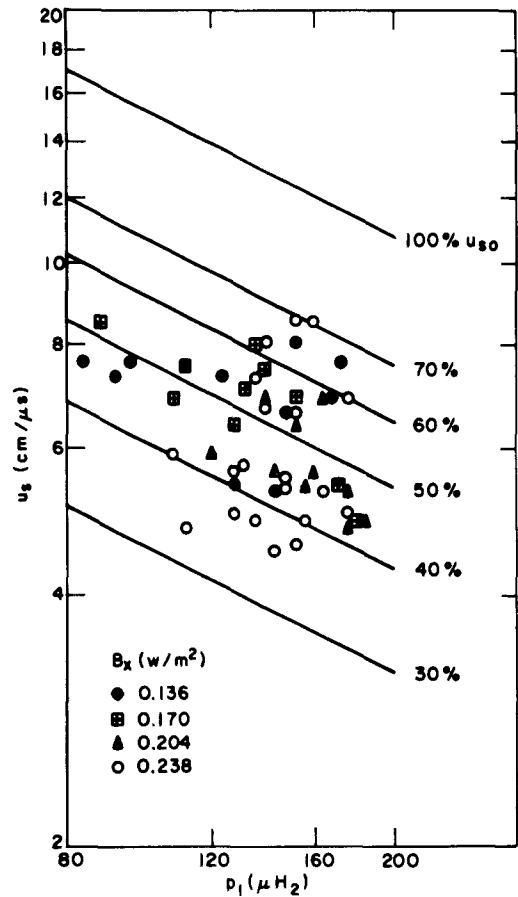


Fig. 19.  $u_s$  and  $u_{s0}$  as functions of  $B_x$  and  $p_1$ ,  $B_x \geq 0.136 \text{ w/m}^2$ .

Although the range of  $p_1$  is too small to allow a definite conclusion to be drawn, the data for any subcritical  $B_x$  indicate that the dependence of  $u_s$  upon  $p_1$  is correctly predicted by Eq. 25. The maximum values of  $u_s$  are found at zero  $B_x$  and are between 80 per cent and 90 per cent of  $u_{s0}$ . It is noted that the predicted range for  $u_s$  at zero  $B_x$  is between 70 per cent and 120 per cent of  $u_{s0}$ . For subcritical, nonzero  $B_x$ ,  $u_s$  tends to decrease as  $B_x$  increases.

The data for critical  $B_x$  exhibit the effect of the narrowed range of  $p_1$  within which well-formed shocks could be obtained. Therefore, no conclusion about the dependence of  $u_s$  upon  $p_1$  can be drawn for critical  $B_x$ .

The dependence of  $u_s$  upon  $p_1$  is removed from consideration by plotting  $u_s/u_{s1}$  against  $B_x$  (Fig. 20).  $u_s/u_{s1}$  does not approach the predicted value of unity; rather, it rapidly decreases as  $B_x$  takes on a nonzero value and gradually diminishes as  $B_x$  further increases. The diminishing of  $u_s/u_{s1}$  with increasing  $B_x$  is probably due to the

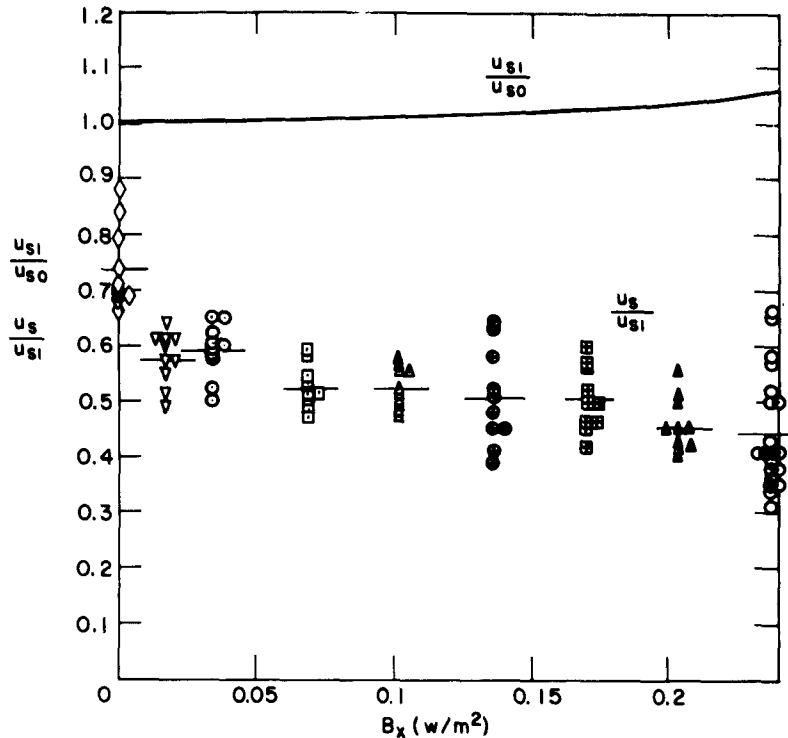


Fig. 20.  $u_s/u_{s1}$  and  $u_{s1}/u_{s0}$  as functions of  $B_x$ .

departure of actual expansion wave behavior from the theory. Several mechanisms exist to cause the departure, all of which are based upon the tendency of the expansion-wave azimuthal velocities to displace the gas radially and increase the frequency of collisions with the outer cylinder. The following phenomena result: (a) The expansion wave gas properties vary with radius, constituting a departure from assumption 1 of the one-dimensional theory; (b) the expansion-wave gas is cooled, with consequent reduction of conductivity, a departure from assumption 4 of the one-dimensional theory; and (c) the expansion-wave azimuthal velocities will be lower than the large velocities predicted by the one-dimensional theory, slowing down the motion of the drive current into the test gas. It might also be conjectured that electrode material contaminates the gas in the expansion wave, increasing the mass that must be accelerated and decreasing the resulting shock velocities.

b. Observed Absolute Spectral Radiant Intensity (Figs. 21-23)

The observed ( $Y_g$ ) and theoretical ( $Y_{g0}$ , Appendix II) values of the test-gas absolute spectral radiant intensity are plotted as functions of  $p_1$  and  $B_x$  for PM I ( $\lambda = 3800 \text{ \AA}$ ) in Figs. 21 and 22 and for PM II ( $\lambda = 5000 \text{ \AA}$ ) in Fig. 23.

The PM I absolute spectral radiant intensity data for subcritical  $B_x$  (Fig. 21)

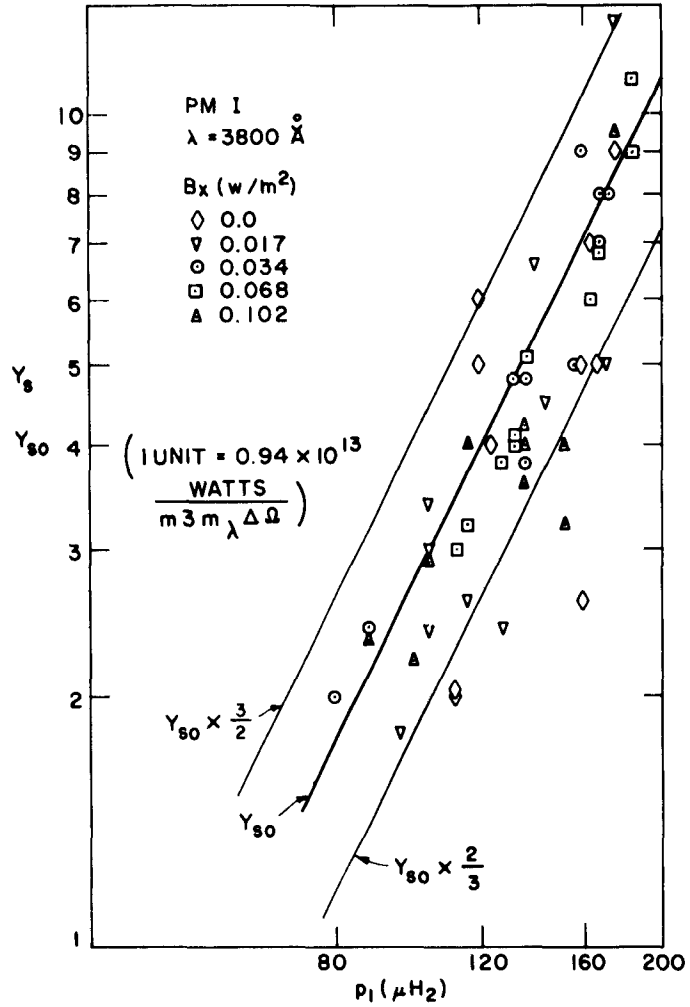


Fig. 21.  $Y_s$  and  $Y_{so}$  as functions of  $B_x$  and  $p_1$ .  
 $B_x \leq 0.102 \text{ w/m}^2$ ,  $\lambda = 3800 \text{ \AA}$ .

confirm the assumptions that  $\rho_4/\rho_1 \approx 4$  and that  $T_4 \approx 3 \times 10^5 \text{ K}$  for all subcritical  $B_x$ . The PM I absolute spectral radiant intensity data for critical  $B_x$  (Fig. 22) exhibit a decrease of observed absolute spectral radiant intensity with increasing  $B_x$ , but it is not possible to confirm the switch-on possibility by using this information alone.

The PM II absolute spectral radiant-intensity data for subcritical  $B_x$  (Fig. 23) disagreed with the theory both in magnitude and functional dependence upon  $p_1$ ,  $Y_s$  being proportional to  $p_1^3$  rather than  $p_1^2$ . The additional radiation was possibly due to line radiation from the impurities present in the test gas. Consequently, PM II was used only to determine  $u_s$ .

It cannot be too strongly emphasized that the absolute spectral radiant intensity

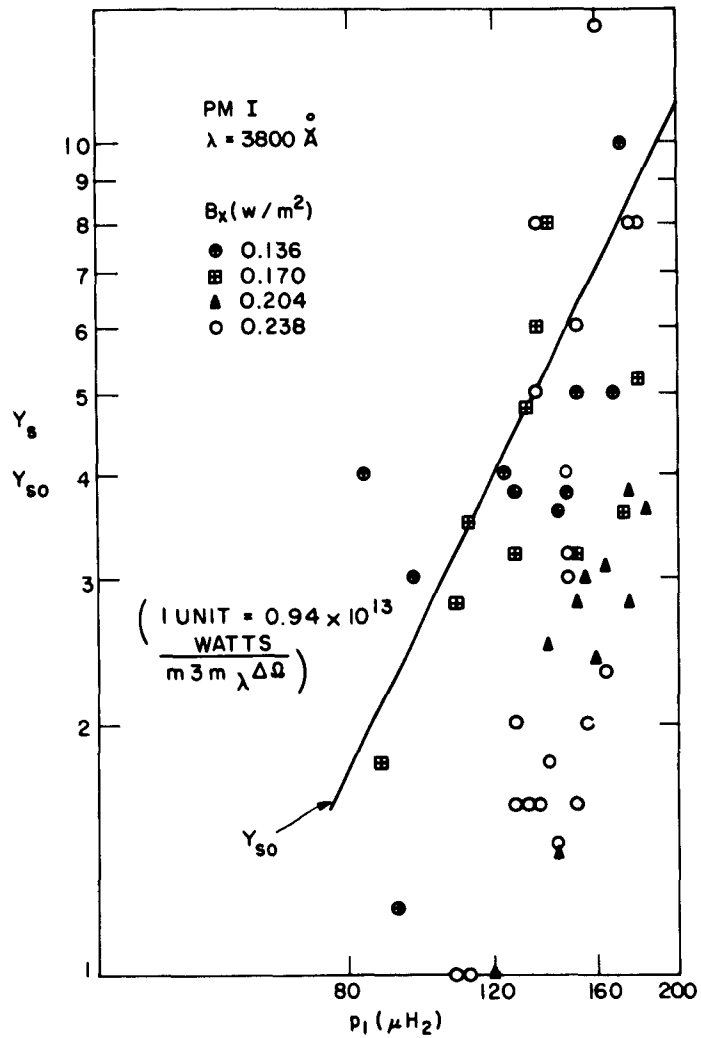


Fig. 22.  $Y_s$  and  $Y_{so}$  as functions of  $B_x$  and  $p_1$ ,  
 $B_x \geq 0.136 \text{ w/m}^2$ ,  $\lambda = 3800 \text{ \AA}$ .

information contained in the discarded well-formed shock data was similar to the retained absolute spectral radiant-intensity data.

c.  $Y_s/Y_{so}$  and  $Y_{s1}/Y_{so}$  vs  $b_{x1}/u_s$  (Figs. 24 and 25)

The decrease of absolute spectral radiant intensity at PM I for critical  $B_x$  suggests the presence of the switch-on shock configuration. Observed shock-velocity data (Figs. 18 and 19) were combined with absolute spectral radiant-intensity data (Figs. 21 and 22) to allow examination of this possibility. Since the test-gas absolute spectral radiant intensity is proportional to the square of the test-gas density (with a fully ionized test

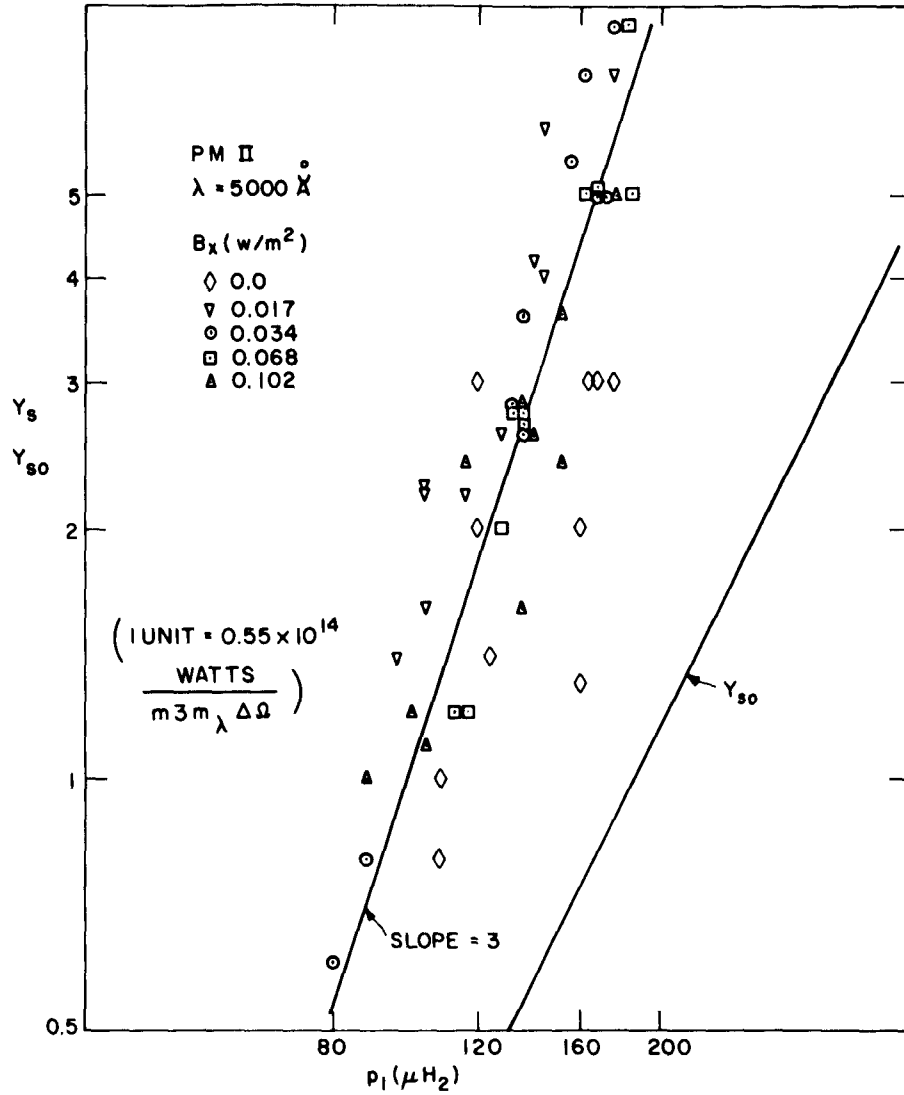


Fig. 23.  $Y_s$  and  $Y_{so}$  as functions of  $B_x$  and  $p_1$ .  
 $B_x \leq 0.102 \text{ w/m}^2$ ,  $\lambda = 5000 \text{ \AA}$ .

gas assumed), and the density ratio is 4 for subcritical  $B_x$ ,

$$\frac{Y_{s1}}{Y_{so}} = \frac{1}{16} \left( \frac{\rho_2}{\rho_1} \right)^2 = \frac{1}{16} \left( \frac{u_s}{b_{x1}} \right)^4 \quad u_s \leq 2b_{x1}. \quad (29)$$

Here, Eq. 15 has been employed. This expression is especially convenient because of the sharp break in the functional dependence of  $\frac{Y_{s1}}{Y_{so}}$  upon  $\frac{u_s}{b_{x1}}$  at  $u_s = 2b_{x1}$ .

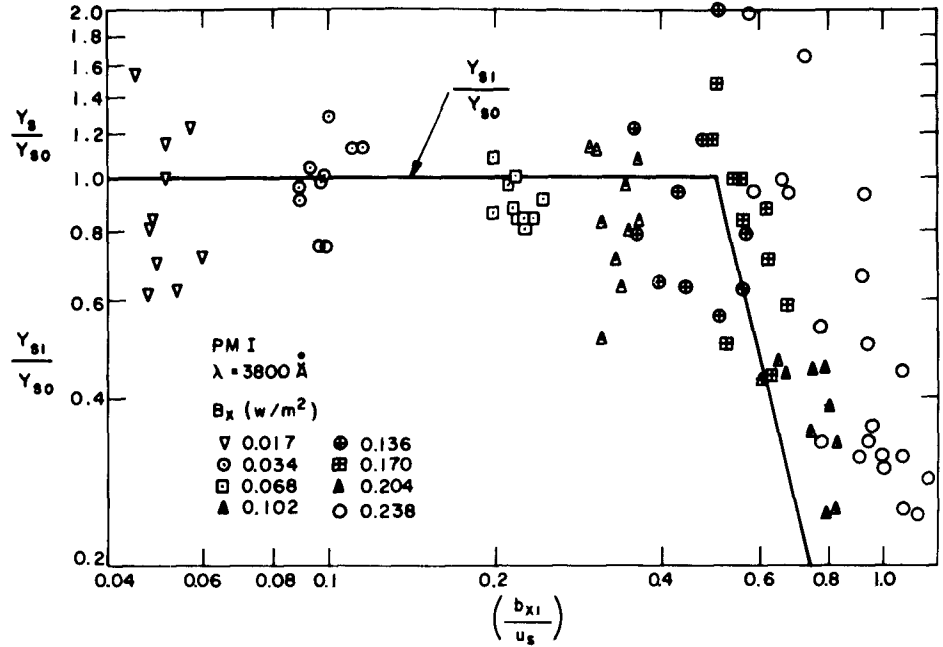


Fig. 24.  $Y_s/Y_{so}$  and  $Y_{sl}/Y_{so}$  as functions of  $b_{x1}/u_s$ ,  $\lambda = 3800 \text{ \AA}$ .

Observed values of  $\frac{Y_s}{Y_{so}}$  and the theoretical curve of  $\frac{Y_{sl}}{Y_{so}}$  are plotted as functions of  $\frac{b_{x1}}{u_s}$  in Figs. 24 and 25. For subcritical  $B_x$ , the observed values of  $\frac{Y_s}{Y_{so}}$  cluster about the theoretical curve in random fashion. The data for subcritical  $B_x$  indicate no discernible functional dependence upon  $u_s$  at any fixed value of  $B_x$ . For any fixed critical  $B_x$  (Fig. 25), however, the data exhibit a slope remarkably close to the theoretical value of -4. The scatter at any fixed critical  $B_x$  and  $b_{x1}/u_s$  does not substantially exceed the scatter at any fixed subcritical  $B_x$  and  $b_{x1}/u_s$ . The major deviation from the theory seems to be only the position of the knee of the curve. It is possible that the experimental points are as much as 10 per cent too far to the right because: (a)  $u_s$  is the average shock velocity during the passage of the shock from PM I to PM II, whereas the absolute light intensity was measured approximately at the maximum shock velocity; and (b) any deviation of the timing sequence from the expected finds  $B_x$  at a value below the maximum value.

In the particular case  $B_x = 0.238 \text{ w/m}^2$ , both a change of the experimental procedure for charging the axial-field current capacitor bank, and the replacement of a component in the metering section of the axial-field capacitor bank power supply may have caused some additional but consistent error.

These data indicate that the switch-on shock is probably the stable configuration

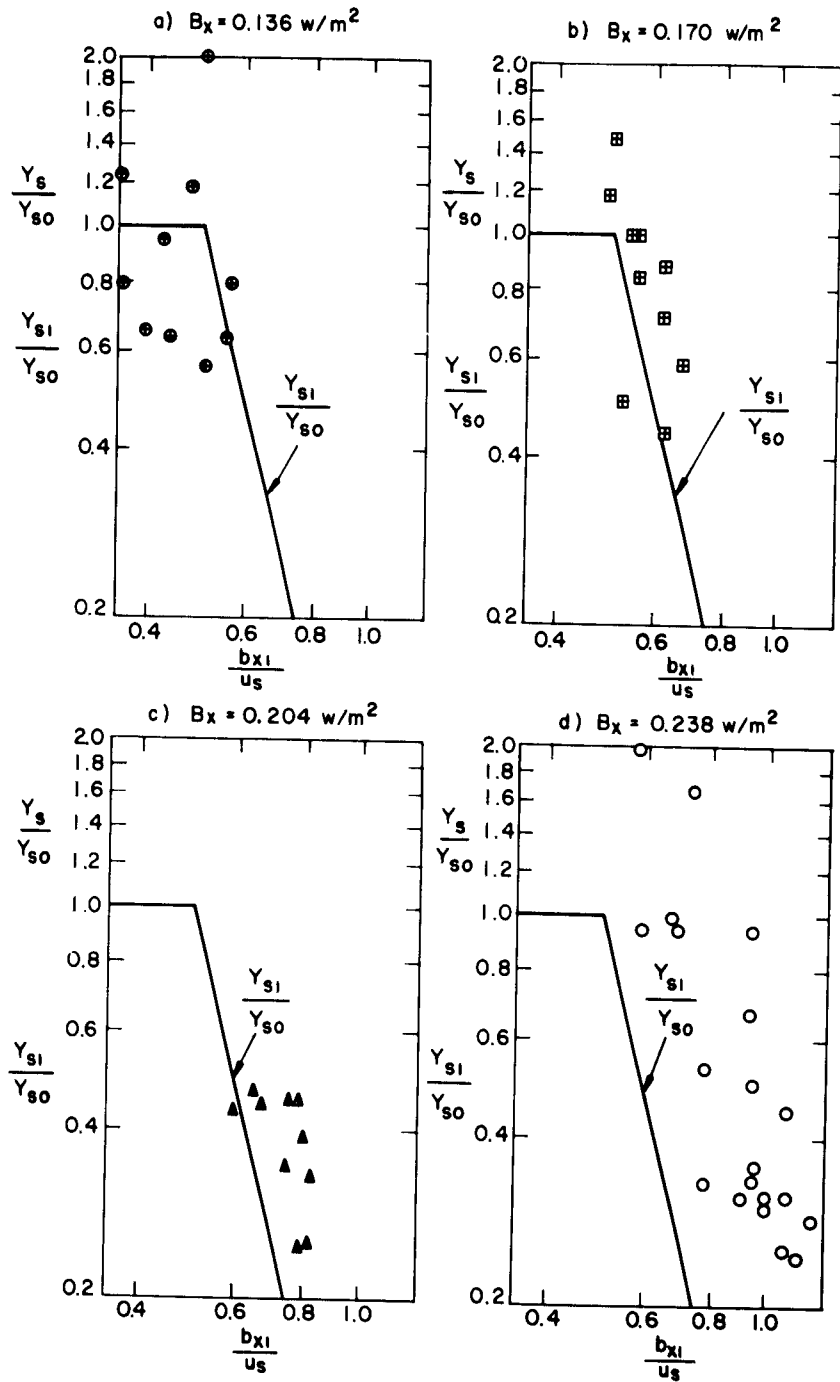


Fig. 25.  $Y_s/Y_{so}$  and  $Y_{s1}/Y_{so}$  as functions of  $bx_1/u_s$  and  $B_x$ ,  
 $B_x \geq 0.136 \text{ w/m}^2$ ,  $\lambda = 3800 \text{ \AA}$ .

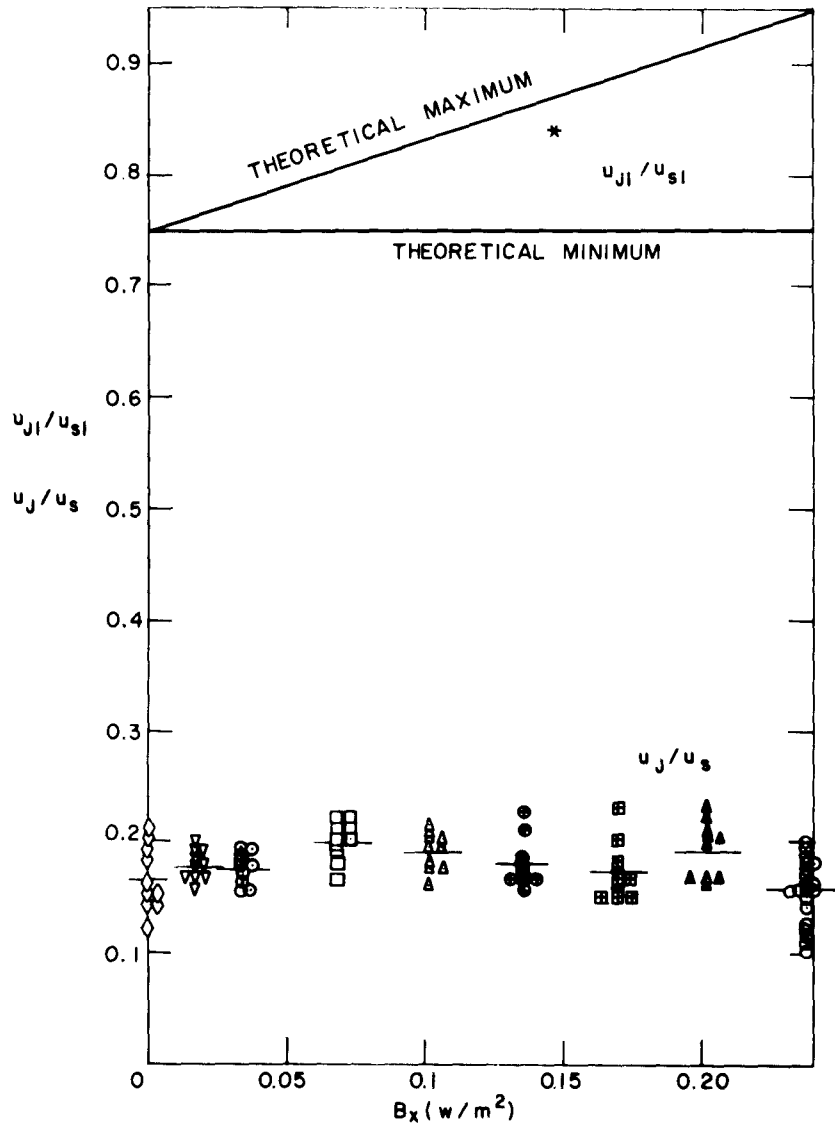


Fig. 26.  $u_J/u_s$  and  $u_{J1}/u_{s1}$  as functions of  $B_x$ .

in this shock tube for  $u_s \leq 2b_{x1}$ .

Note that the one-dimensional shock-wave theory predicts<sup>1</sup> that the switch-on shock can only occur for  $B_x/B_{y0} \geq 0.453$  ( $B_x/\sqrt{B_{y0}^2 + B_x^2} \geq 0.412$ ), although it was observed to occur for  $B_x/B_{y0} > 0.24$ . This discrepancy exists because  $u_s \neq u_{s1}$ , as the theory has assumed, but  $u_s \sim 0.5u_{s1}$ .

d. Pseudo-Current Velocity (Fig. 26)

The observed pseudo-current velocity (from Eq. 28) was found to diminish with increasing  $B_x$ ; therefore, the value  $u_J/u_s$  was formed and plotted against  $B_x$  in Fig. 26.

The one-dimensional theory shows that  $u_{J1}/u_{s1}$  must lie between  $\frac{3}{4}$  and  $\frac{b_{x4}}{u_{s1}} + \frac{3}{4}$ . The neglect of the small difference between  $u_{s1}$  and  $u_{s0}$  results in the theory placing the

upper limit at  $\frac{3}{4} + \sqrt{\frac{3}{8} \frac{B_x}{B_{y0}}}$ , as shown in Fig. 26. Kemp and Petschek<sup>1</sup> allow the

precise value of  $u_{J1}/u_{s1}$  to be computed at  $B_x = 0.146 \text{ w/m}^2$ , as is indicated in Fig. 26 by an asterisk. As expected, it is close to the upper limit.

The observed values of  $u_J/u_s$  are remarkable in two respects. First,  $u_J/u_s$  is virtually constant for all  $B_x$ . Second, the average value of  $u_J/u_s$  is never in excess of 25 per cent of  $u_{J1}/u_{s1}$ . These two facts indicate a strong spreading of the current sheet and confirm the many previous suspicions about the nature of the deviation of the expansion-wave properties from one-dimensional theory.

Experiments were terminated at  $B_x = 0.238 \text{ w/m}^2$  because the absolute spectral radiant intensity signal was diminishing, and the range of useful  $p_1$  was vanishing.

## V. CONCLUSIONS AND RECOMMENDATIONS

Magnetically driven shock-tube performance has been examined from the standpoint of two separate phenomena, the shock layer and the drive current carrying expansion wave. Despite many departures from the simplified, one-dimensional theory, including

(a.) non-steady flow

$$(b.) \frac{2(r_o - r_i)}{r_o + r_i} \neq 0$$

(c.) a real gas as the working fluid

(d.) finite and nonscalar electrical conductivity

(e.) viscosity effects in the boundary layer,

experimental observations indicate that the one-dimensional theory is adequate for estimating the actual performance in the annular geometry shock tube.

Shock waves were found to exist with  $u_s \leq 2b_{x1}$  in spite of stability considerations to the contrary. The shock transitions were observed, on the basis of measured values of  $B_x$ ,  $\rho_1$ ,  $u_s$  and  $\rho_2$  or  $\rho_4$ , to adhere reasonably well to both the one-dimensional shock-wave theory and the evolutionary shock-wave stability theory even in the switch-on range of axial magnetic fields. Well-formed shocks were not observed in every experiment; the cause of these failures appeared to be associated with the drive current breakdown characteristics.

The deviation of these conditions from the assumptions of one-dimensional theory and the influence of the axial field were observed from the relation of  $u_s/u_{s1}$  and  $u_j/u_s$  to  $B_x$  to influence strongly the expansion wave behavior. Although  $u_s/u_{s1}$  was within the expected limits for zero axial magnetic field, it continuously decreased as the axial field magnitude increased. The observation that  $u_j/u_s$  was fairly constant for all values of axial field but was less than one-quarter of the predicted value, reveals that the drive current spreads throughout the shock tube rather than concentrating at the upstream edge of the expansion wave as the one-dimensional theory predicts.

The effect of boundary-layer leakage upon test duration and shock velocity was predicted on the basis of a simple model and largely confirmed in these experiments.

Since this experiment is only one in a continuing program of magnetically driven shock-tube development, several recommendations are included to help direct the future effort.

1. If the operation of the shock tube is to be understood, it is necessary to explain the actual behavior of the expansion wave. The complete expansion-wave problem is extremely complex and theoretically intractable, but the important deviations from one-dimensional expansion wave theory might be explained by means of models that include only one additional constraint (for example, maximum attainable azimuthal velocity).

2. In order to increase the reliability of the shock tube and the reproducibility of the experimental observations, arc theory should be considered in an effort to improve

the breakdown behavior. It is possible that the substitution of a different experimental gas would be an improvement, even though the shock velocity decreased.

3. The observed test duration was quite small ( $\sim 0.5 \mu\text{sec}$ ), and few experiments can be completed within this period. Theoretically, the maximum test duration for this experiment is  $\sim 2 \mu\text{sec}$ , and attempts should be made to approach this value.

4. The knowledge of any local test gas and expansion-wave properties would contribute significantly to an understanding of the shock-tube performance. Devices that indicate any possibility of success in this application should be thoroughly investigated.

5. Complicated flow patterns can often be deciphered from smear photographs. The current photographic technology is such that smear photographs can be made of the test gas in this experiment, and the possibility of obtaining such information should not be overlooked in future experiments.

## APPENDIX I

### ESTIMATES OF THE TEST DURATION

#### 1. MINIMUM TEST DURATION

The drive-current pressure is proportional to  $1/r^2$  (Eq. 24), causing the upstream edge of the expansion wave to bend downstream with increasing radius, with the result that a finite volume of test gas exists even when the drive current overtakes part of the

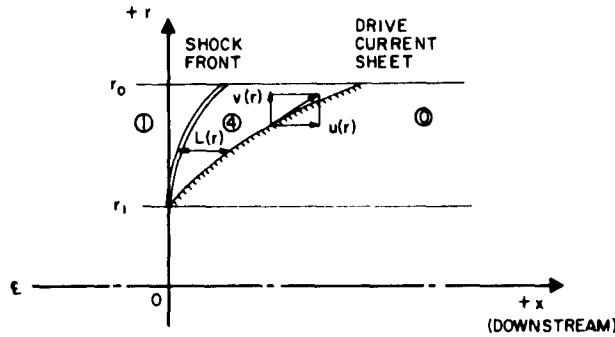


Fig. 27. Coordinate system for estimation of test duration.

shock front.<sup>6</sup> An estimate of the extent of this minimum test-gas volume is made by using the nomenclature of Fig. 27 and assuming<sup>6</sup>:

- (i) steady flow (shock front and expansion wave move with equal velocities);
- (ii) an impenetrable drive-current interface (the flow direction is parallel to the interface);
- (iii)  $L(r)$  is small enough to insure that all properties are functions of  $r$  alone;
- (iv) the axial magnetic field is zero;
- (v)  $\rho_4 = \left( \frac{k_4 + 1}{k_4 - 1} \right) \rho_1$ ;
- (vi)  $\rho_1 u_1^2 \approx \frac{B_i^2}{2\mu}$ ;
- (vii)  $u_4 = L = 0$  at  $r = r_1$  (the drive current has overtaken the shock front);
- (viii)  $v_4$  may have any value at  $r = r_0$  (Appendix I.2 shows that the outer wall behaves as a sink for the gas);
- (ix)  $\frac{r}{r_1} \rightarrow 1$ .

Defining

$$a = \rho_4 v_4 L r \tag{30}$$

and

$$\beta = \rho_4 v_4 L r u_4 = a u_4, \tag{31}$$

we have the conservation equations

$$\frac{d}{dr} (a) = \rho_1 u_1 r \tag{continuity} \tag{32}$$

$$\frac{d}{dr} (\beta) = \rho_1 u_1^2 r \left\{ 1 - \left( \frac{r_i}{r} \right)^2 \right\} \quad (\text{x-momentum}) \quad (33)$$

$$\frac{d}{dr} (\alpha v_4) = \rho_1 u_1^2 \left\{ \frac{r_i^2}{r} \frac{u_4}{v_4} - \frac{d}{dr} \left( \frac{r_i^2}{r} L \right) \right\} \quad (\text{r-momentum}) \quad (34)$$

Equations 32 and 33 can be integrated directly to yield

$$\alpha = \frac{\rho_1 u_1^2 r_i^2}{2} \left\{ \left( \frac{r}{r_i} \right)^2 - 1 \right\} \quad (35)$$

$$\beta = \frac{\rho_1 u_1^2 r_i^2}{2} \left\{ \left( \frac{r}{r_i} \right)^2 - 1 - \ln \left( \frac{r}{r_i} \right)^2 \right\} \quad (36)$$

Since  $u_4 = \beta/\alpha$  (Eq. 31), and  $r/r_i \rightarrow 1$ , it follows that

$$u_4 = u_1 \left\{ 1 - \frac{2 \ln \left( \frac{r}{r_i} \right)}{\left( \frac{r}{r_i} \right)^2 - 1} \right\} \approx u_1 \left\{ \frac{\left( \frac{r}{r_i} \right)^2 - 1}{\left( \frac{r}{r_i} \right)^2 + 1} \right\} \quad (37)$$

and also that

$$\beta \approx \rho_1 u_1^2 r_i r \left( \frac{r}{r_i} - 1 \right)^2 \quad (38)$$

By neglecting  $\frac{d}{dr} \left( \frac{r_i^2 L}{r} \right)$  in comparison with  $\frac{r_i^2 u_4}{r v_4}$  in Eq. 34 (an approximation which can be shown to be valid for  $r/r_i > 1.1$ ), (34) becomes

$$\frac{d}{dr} (\alpha v_4)^2 \approx \frac{2 \rho_1 u_1^2 r_i^2}{r} \approx 2 (\rho_1 u_1^2)^2 r_i^3 \left( \frac{r}{r_i} - 1 \right)^2 \quad (39)$$

which may be integrated to yield

$$\alpha v_4 \approx \sqrt{\frac{2}{3}} \rho_1 u_1^2 r_i^2 \left( \frac{r}{r_i} - 1 \right)^{3/2}, \quad (40)$$

whence

$$v_4 \approx \sqrt{\frac{8}{3}} \frac{\left( \frac{r}{r_i} - 1 \right)^{1/2}}{\left( \frac{r}{r_i} + 1 \right)} u_1. \quad (41)$$

Also

$$\frac{L}{r_i} = \frac{\alpha}{\rho_4 v_4 r_i r} \approx \left( \frac{k_4 - 1}{k_4 + 1} \right) \sqrt{\frac{3}{32}} \left( \frac{r_i}{r} \right) \left( \frac{r}{r_i} + 1 \right)^2 \left( \frac{r}{r_i} - 1 \right)^{1/2}. \quad (42)$$

Note that the gas properties enter into the equation only for  $L(r)$ . Since  $dx_j/dr = u_4/v_4$ ,

$$\frac{dx_J}{dr} \approx \frac{\sqrt{\frac{3}{8}} \left(\frac{r}{r_i} + 1\right)^2 \left(\frac{r}{r_i} - 1\right)^{1/2}}{\left(\frac{r}{r_i}\right)^2 + 1} \approx \sqrt{\frac{3}{2} \left(\frac{r}{r_i} - 1\right)}. \quad (43)$$

Equation 43 may be integrated to yield

$$\frac{x_J}{r_i} \approx \sqrt{\frac{2}{3} \left(\frac{r}{r_i} - 1\right)^{3/2}}. \quad (44)$$

This equation is compared below with the data of Keck, Fishman, and Petschek<sup>6</sup> as a rough check of the validity of the assumptions used in the derivations above.

$\frac{r}{r_i}$	$\frac{x_J}{r_i}$ (Eq. 44)	$\frac{x_J}{r_i}$ (Keck, et al. <sup>6</sup> )
1	0	0
1.5	0.29	0.2 - 0.4
2.0	0.82	0.6 - 0.9
2.5	1.50	1.2 - 2.0

The agreement between the computed and observed values is excellent, whence it may be concluded that this model properly describes the flow pattern when the drive current overtakes the shock front, because of the variation of pressure with radius. The other important properties are presented below for  $k_4 = 5/3$  and for the range of values of  $r/r_i$  found in the shock tube investigated here. They are valid only for  $r/r_i > 1.1$ , because of the assumption that  $\frac{d}{dr} \left(\frac{r_i^2}{r}\right) \ll \frac{r_i^2}{r} \frac{u_4}{v_4}$ .

$\frac{r}{r_i}$	$\frac{x_J}{r_i}$ (Eq. 44)	$\frac{L}{r_i}$ (Eq. 42)	$\frac{x_s}{r_i} = \frac{x_J}{r_i} - \frac{L}{r_i}$ (shock front)
1	0	0	0
1.1	0.03	0.10	-0.07
1.2	0.07	0.14	-0.07
1.3	0.13	0.17	-0.04
1.4	0.20	0.20	-0.00

The predicted values of  $x_s/r_i$  in the range of validity of  $r/r_i$  indicate that the shock front is tilted slightly downstream with increasing radius. The average angle of shock-front tilt between  $r/r_i = 1.1$  and  $r/r_i = 1.4$  is approximately  $10^\circ$  (a value that is

independent of  $u_g$ ). The time required for the shock front to pass a given axial point would be approximately  $0.07 r_i/u_g < 0.1 \mu s$  for this experiment. The minimum length of the test-gas volume at the mean radius ( $r/r_i = 1.2$ ) is taken to be the appropriate measure of the minimum length of the test-gas slug, and this length has the value  $\sim 0.7$  cm for this experiment.

## 2. MAXIMUM TEST DURATION

Roshko<sup>8</sup> and Duff<sup>9</sup> have shown that the transfer of test gas into the boundary layer prevents the test-gas volume in combustion-driven shock tubes from increasing indefinitely. Since the test gas that condenses on the wall of the magnetically driven shock tube suffers a large decrease in conductivity, the condensed gas therefore leaks past the drive current without difficulty, and a phenomenon similar to that observed in combustion-driven shock tubes can result. Following Roshko,<sup>8</sup> (using the nomenclature of Fig. 27), but limiting the derivation to strong gasdynamic shocks ( $M_1 = \infty$ ) in hydrogen and neglecting any boundary layer mass transfer at  $r = r_i$  (assuming the drive-current configuration of Appendix I.1), we can make an estimate of the maximum test-gas volume.

Since

$$\dot{m}_c = 2\pi r_o \sqrt{\rho_{4W} \mu_{4W} u_1 L_o}, \quad (45)$$

where  $\dot{m}_c$  is the rate of mass transfer out of the test-gas volume,  $\mu$  is the dynamic viscosity, and  $W$  refers to conditions at the outer wall of the shock tube, and

$$\mu_{4W} \approx \mu_1 \sqrt{\frac{T_{4W}}{T_1}} \approx \mu_1 \quad (\text{approximate Sutherland law}^{11}) \quad (46)$$

$$\rho_{4W} = \frac{\rho_4 T_4}{T_{4W}} \approx \frac{4\rho_1 T_4}{T_1} \quad (\text{perfect gas}) \quad (47)$$

$$T_4 \approx \frac{3}{16} \frac{u_1^2}{R_4} \quad (\text{Eq. 13}), \quad (48)$$

it follows therefore that

$$\dot{m}_c = \pi \sqrt{3} r_o \sqrt{\frac{\rho_1 \mu_1 u_1^3 L_o}{R_4 T_1}}. \quad (49)$$

The rate of mass transfer into the test-gas volume is referred to as  $\dot{m}_s$ , and is given by the relation

$$\dot{m}_s = \rho_1 \pi (r_o^2 - r_i^2) \left( u_1 + \frac{dL_o}{dt} \right). \quad (50)$$

At equilibrium,  $dL_o/dt = 0$ ,  $L_o = L_{oe}$ , and  $\dot{m}_g = \dot{m}_c$ , whence

$$L_{oe} \approx \frac{\rho_1 R_4 T_1}{3\mu_1 u_1} r_o^2 \left\{ 1 - \left( \frac{r_i}{r_o} \right)^2 \right\}^2 \quad (51)$$

For this experiment,  $L_{oe} \approx 4$  cm. Since the value of  $L_{oe} \approx 4$  cm is somewhat larger than the value obtained in section 1 for the minimum length of the test-gas volume ( $L_o \approx 0.7$  cm), the conclusion is therefore drawn that the shock wave separates from the drive-current interface, but that the shock phenomenon retains some of the features predicted above (e.g., the downstream tilting of the shock front and current interface with increasing radius).

The amount of time required for equilibrium between  $\dot{m}_c$  and  $\dot{m}_g$  to be established (under the assumption of a step-function change in the shock velocity) is given by

$$t_e \approx \frac{6L_{oe}}{u_1} \approx 2.5 \mu s, \quad (52)$$

where  $L_o > 0.7 L_{oe}$  for  $t > t_e$ . Consequently, equilibrium should be established by the time the shock front reaches PMI ( $t \sim 5 \mu s$ ), and the anticipated experimental value of the test-gas slug length is therefore  $\sim 4$  cm.

The removal of test gas by the boundary layer causes the drive-current interface to accelerate and the shock to decelerate until they travel at equal velocities. The equilibrium value of this velocity is estimated by means of the simple model described below.

In a reference frame attached to the shock front and current interface, the conservation of axial momentum at equilibrium is expressed by the relation

$$\begin{aligned} \rho_1 u_1^2 \pi (r_o^2 - r_i^2) + \text{skin friction that is due to moving wall} \\ = p_4 \pi (r_o^2 - r_i^2) + \text{x-momentum outflow associated with } \dot{m}_c \end{aligned} \quad (53)$$

In this reference frame the wall velocity is equal to  $u_1$ , and is greater than  $4u_{4W}$ . Consequently, the test gas appears to be standing still, and any x-momentum imparted to the test gas in the boundary layer appears to be the result of the skin friction, that is,

$$\text{skin friction} \approx \text{outflow associated with } \dot{m}_c. \quad (54)$$

Therefore

$$u_1 = \sqrt{\frac{p_4}{\rho_1}}. \quad (55)$$

Since the ideal gasdynamic relation (Eq. 23) is

$$u_1 = 1.16 \sqrt{\frac{p_4}{\rho_1}}, \quad (56)$$

it may be concluded that the loss of test gas to the boundary layer results in a 14 per cent decrease of the observed shock velocity from the theoretical shock velocity based upon  $p_4$  and  $\rho_1$ . This 14 per cent decrease in the observed shock velocity is apparent in the data of experiments conducted by Duff.<sup>9</sup>

## APPENDIX II

### ABSOLUTE SPECTRAL RADIANT-INTENSITY INFORMATION

#### 1. ABSOLUTE SPECTRAL RADIANT INTENSITY OF FULLY IONIZED HYDROGEN FOR ZERO MAGNETIC FIELD

Janes and Koritz<sup>12</sup> numerically calculated the absolute Bremsstrahlung spectral radiant intensity ( $Y_{so}$  = energy/volume/spherical angle/wavelength/time) for the temperature and wavelength ranges of this experiment and zero magnetic field, and the calculations are reproduced on Fig. 28 ( $\lambda = 3800 \text{ \AA}$ ) and Fig. 29 ( $\lambda = 5000 \text{ \AA}$ ). The computed results clearly indicate that  $Y_{so}$  is proportional to the test-gas electron number density ( $n$ ) squared, and that  $Y_{so}$  is only a weak function of the test-gas temperature ( $T$ ). In fact, assuming that  $T \approx 3 \times 10^5 \text{ K}$ ,<sup>7</sup> we find that the value  $Y_{so}/n^2 = 3.1 \times 10^{-33}$  for  $\lambda = 3800 \text{ \AA}$  is accurate within 10 per cent for  $5 \times 10^4 < T < 5 \times 10^5$ , and the value  $Y_{so}/n^2 = 2.0 \times 10^{-33}$  for  $\lambda = 5000 \text{ \AA}$  is accurate within 10 per cent for  $5 \times 10^4 < T < 4 \times 10^5$ .

Oster<sup>13</sup> has derived the following analytical expressions for  $Y_{so}/n^2$ , based upon the assumption that the radiating electrons move in straight lines:

$$\frac{Y_{so}}{n^2} = \frac{a}{\lambda^2 \sqrt{T}} \ln(\beta \lambda T^{3/2}) \quad (\text{classical range}) \quad (57)$$

$$\frac{Y_{so}}{n^2} = \frac{a}{\lambda^2 \sqrt{T}} \ln(\gamma \lambda T) \quad (\text{quantum range}) \quad (58)$$

Here,  $a = 0.90 \times 10^{-43}$ ,  $\beta = 1.65 \times 10^{-1}$ , and  $\gamma = 1.55 \times 10^{+2}$ . The classical range is  $T \leq (\gamma/\beta)^2$ , and the quantum range is  $T \geq (\gamma/\beta)^2$ . Both expressions are valid only for  $T \gg 1.5/(\lambda)^{2/3} \sim 3 \times 10^4 \text{ K}$ .

Referring to Figs. 28 and 29, it is apparent that the computed and analytical methods of computing  $Y_{so}/n^2$  agree for  $T > 3 \times 10^5 \text{ K}$ . The analytical formulation has the additional advantage of allowing  $T$  and  $n^2$  to be directly computed from the values of  $Y_s$  at two separate wavelengths (I and II), as follows:

$$T = \left\{ \frac{1}{\beta} (\lambda_I \lambda_{II}^{-\Gamma})^{\frac{1}{\Gamma-1}} \right\}^{2/3} \quad (\text{classical range}) \quad (59)$$

$$T = \frac{1}{\gamma} (\lambda_I \lambda_{II}^{-\Gamma})^{\frac{1}{\Gamma-1}} \quad (\text{quantum range}) \quad (60)$$

$$n^2 = \frac{Y_{sI}}{a \sqrt{\beta}} \left( \frac{\Gamma-1}{\Gamma} \right) \frac{\lambda_I^{\left( \frac{6\Gamma-5}{3\Gamma-3} \right) - \left( \frac{\Gamma}{3\Gamma-3} \right)} \lambda_{II}}{\ln \left( \frac{\lambda_I}{\lambda_{II}} \right)} \quad (\text{classical range}) \quad (61)$$

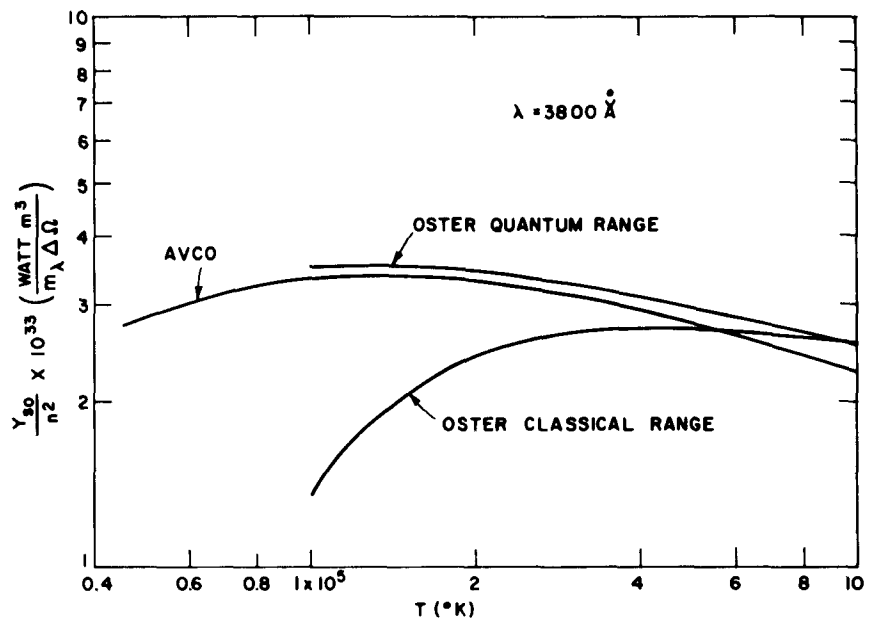


Fig. 28.  $Y_{SO}/n^2$  as a function of  $T$ ,  $\lambda = 3800 \text{ \AA}$ .

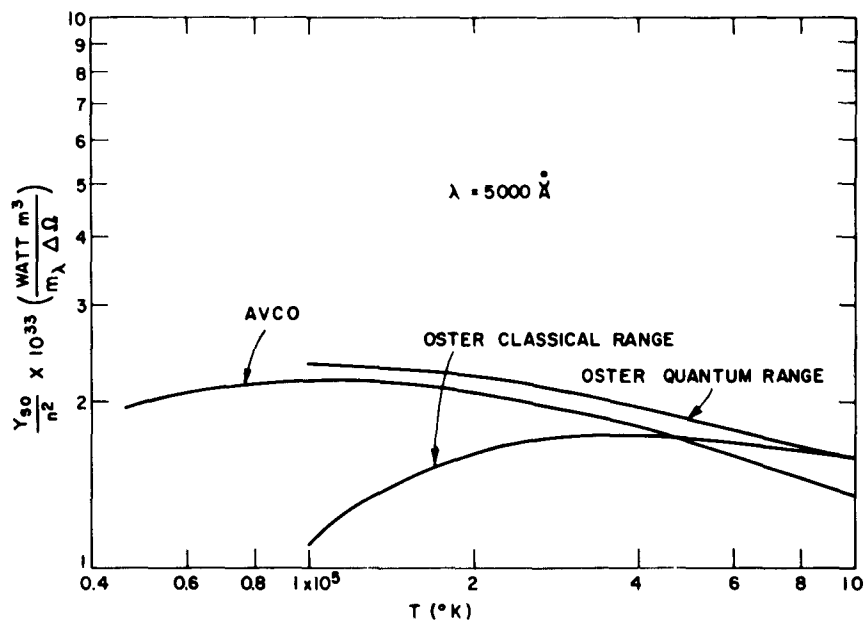


Fig. 29.  $Y_{SO}/n^2$  as a function of  $T$ ,  $\lambda = 5000 \text{ \AA}$ .

$$n^2 = \frac{Y_{sI}}{\alpha\sqrt{Y}} \left(\frac{\Gamma-1}{\Gamma}\right) \frac{\lambda_I^{\left(\frac{4\Gamma-3}{2\Gamma-2}\right)} \lambda_{II}^{-\left(\frac{\Gamma}{2\Gamma-2}\right)}}{\ln\left(\frac{\lambda_I}{\lambda_{II}}\right)} \quad (\text{quantum range}) \quad (62)$$

where

$$\Gamma = \frac{Y_{sI}\lambda_I^2}{Y_{sII}\lambda_{II}^2}$$

## 2. COMPUTATION OF THE OBSERVED ABSOLUTE SPECTRAL RADIANT INTENSITY

The absolute spectral radiant intensity of the test gas was calculated by comparing the observed photomultiplier signal with the signal that is due to a source of known intensity, as described below.

Barbrow<sup>14</sup> has described a method for computing, with 5 per cent accuracy, the spectral radiant intensity ( $W = \text{energy/spherical angle/wavelength/time}$ ) of a tungsten filament incandescent lamp of known radiant flux ( $P = \text{energy/time}$ ) and approximate filament temperature. Forsythe<sup>15</sup> provides the data that establish the facts that

$$\begin{aligned} W_{cI} &= 3.6 \times 10^4 P \\ W_{cII} &= 3.6 \times 10^5 P, \end{aligned} \quad (63)$$

where  $c$  refers to the calibration value,  $\lambda_I = 3800 \text{ \AA}$ , and  $\lambda_{II} = 5000 \text{ \AA}$ .

Neglecting reflection, refraction, etc., we have

$$W_{so} = Y_{so} \Delta V, \quad (64)$$

where  $\Delta V$  is a small volume of test gas distant from and visible to the photomultiplier.

Since  $V_{so}/V_c = W_{so} \Delta \Omega_{so} / W_c \Delta \Omega_c$ , where  $V$  is the photomultiplier output signal, and  $\Delta \Omega$  is the spherical angle of radiation intercepted by the photomultiplier optical system, it follows that

$$\frac{V_{so}}{V_c} = \frac{Y_{so} \Delta V \Delta \Omega_{so}}{W_c \Delta \Omega_c}. \quad (65)$$

Under the assumptions of a compression ratio of 4 across the shock and complete ionization of the test gas,  $n^2 = 8.0 \times 10^{40} p_1^2$  ( $p_1$  in  $\mu$ ),<sup>11</sup> and therefore from Appendix II it follows that

$$\begin{aligned}
 Y_{\text{soI}} &= 2.5 \times 10^8 p_1^2 \\
 Y_{\text{soII}} &= 1.6 \times 10^8 p_1^2.
 \end{aligned}
 \tag{66}$$

The method of calibration (section 3.2) fixes  $V_c = 0.40$  and  $\Delta\Omega_c = \Delta\Omega_{\text{so}}$ . Since  $P = 0.94$ ,  $\Delta V_I = 0.91 \times 10^{-8}$ , and  $\Delta V_{II} = 1.54 \times 10^{-8}$ , it follows that

$$\begin{aligned}
 V_{\text{soI}} &= 2.7 \times 10^{-5} p_1^2 \\
 V_{\text{soII}} &= 2.9 \times 10^{-6} p_1^2
 \end{aligned}
 \tag{67}$$

( $p_1$  in  $\mu$ )

If the observed photomultiplier signal magnitude is  $V_s$ , then

$$\frac{Y_s}{Y_{\text{so}}} = \frac{V_s}{V_{\text{so}}}
 \tag{68}$$

Except when otherwise noted, the units above are mks.

## APPENDIX III

### AUXILIARY EQUIPMENT

#### Vacuum Equipment

- 1 National Research Corporation H-2-SP diffusion pump
- 1 National Research Corporation MO-76390 molecular trap
- 1 National Research Corporation 520 ionization gauge
- 1 W. M. Welch Manufacturing Company 1402B mechanical pump
- 1 Vacuum Engineering Corporation VL variable leak valve

#### Power Supplies

- 2 New Jersey Engineering Corporation H-10-50 power supplies
- 1 Potter Company PHV30-IM60V power supply

#### Capacitance

- 43 Aerovox Corporation PX50J5 capacitors
- 12 Aerovox Corporation PX50D4 capacitors
- 4 Cornell-Dubilier Electronics 30-DK-T5 capacitors

#### Triggering Equipment

- 1 Dumont Corporation 404 pulse generator
- 3 Avco Corporation designed 1.5 KV pulse generators
- 1 M.I.T. designed 100-300  $\mu$ sec delay circuit
- 3 Laboratory for Electronics, Inc., T-71358-2 pulse transformers

#### Photomultiplier Equipment

- 2 Radio Corporation of America 1P21 photomultipliers
- 2 Northeast Scientific Corporation RE-1602 power supplies
- 2 Avco designed photomultiplier circuits
- 1 Bausch and Lomb, Inc., 33-78-38 second-order interference filter
- 1 Bausch and Lomb, Inc., 33-78-50 second-order interference filter
- 2 Corning Glass Works 4308 cutoff filters
- 1 Electrical Testing Laboratories, Inc., 8103 standard lamp

#### Oscilloscopes

- 1 Tektronix, Inc., 555 dual-beam oscilloscope
- 2 Tektronix, Inc., Type G preamplifiers
- 1 Tektronix, Inc., 551 dual-beam oscilloscope
- 2 Tektronix, Inc., Type L preamplifiers
- 1 Tektronix, Inc., 535 single-beam oscilloscope
- 1 Tektronix, Inc., Type B preamplifier

#### Acknowledgment

The author wishes to express deep appreciation to Professor A. H. Shapiro, Professor Sanborn C. Brown, and Professor J. A. Fay for their support and encouragement of this research; to Dr. J. E. Anderson for numerous interesting discussions that led to the choice of this topic for investigation; to Mr. John B. Heywood and Mr. Miklos Sajben for their generous cooperation in the laboratory; and to the Avco-Everett Corporation for providing the information required for the construction and operation of the shock tube used in these experiments.

## References

1. N. H. Kemp and H. E. Petschek, Theory of Flow in the Magnetic Annular Shock Tube, Avco Research Report No. 60, Everett, Massachusetts, July 1959.
2. J. E. Anderson, Magneto-hydrodynamic Shock Waves (The M.I.T. Press, Cambridge, Mass., in press).
3. J. A. Shercliff, One-dimensional magnetogasdynamics in oblique fields, *J. Fluid Mech.* 9, 481 (1960).
4. R. M. Patrick, The Production and Study of High Speed Shock Waves in a Magnetic Annular Shock Tube, Avco Research Report No. 59, Everett, Massachusetts, July 1959.
5. E. R. Pugh, Studies of the Phenomena Occurring in an Electromagnetic Shock Tube, Graduate School of Aeronautical Engineering Report, Cornell University, Ithaca, New York, 1962.
6. J. C. Keck, F. Fishman, and H. E. Petschek, Current Distribution and Flow Model for Large Radius-Ratio MAST, Avco Research Report No. 117, Everett, Massachusetts, January 1962.
7. W. Weise, H. Riez, and H. Griem, Measurements of temperatures and densities in shock-heated hydrogen and helium plasmas, *Phys. Rev.* 120, 1079 (1960).
8. A. Roshko, On flow duration in low pressure shock tubes, *Phys. Fluids* 3, 835 (1960).
9. R. E. Duff, Shock tube performance at low initial pressure, *Phys. Fluids* 2, 214 (1959).
10. L. Spitzer, Jr., Physics of Fully Ionized Gases (Interscience Publishers, Inc., New York, 1957).
11. J. H. Jeans, An Introduction to the Kinetic Theory of Gases (Cambridge University Press, 1952).
12. G. S. Janes and H. E. Koritz, Numerical Calculation of Absolute Bremsstrahlung Intensity for a Fully Ionized Fully Dissociated Hydrogenic Gas, Avco Research Report No. 70, Everett, Massachusetts, September 1959.
13. L. Oster, Emission, absorption, and conductivity of a fully ionized gas at radio frequencies, *Revs. Modern Phys.* 33, 525 (1961).
14. L. E. Barbrow, Memorandum on a procedure for obtaining spectral radiant intensities of tungsten-filament lamps, 400-700 m $\mu$ , *J. Opt. Soc. Am.* 49, 1122 (1959).
15. W. E. Forsythe, Smithsonian Physical Tables (Smithsonian Institution Press, Washington, D.C., 9th edition, 1956), p. 120.